

MASARYKOVA UNIVERZITA
Přírodovědecká fakulta
Ústav teoretické fyziky a astrofyziky



DIPLOMOVÁ PRÁCE
Studium mikrokvasarů

Ondřej Kamenský

Školitel: Mgr. Filip Hroch, Ph.D.

2016

Bibliografický záznam

Autor: Ondrej Kamenský
Přírodovědecká fakulta, Masarykova univerzita
Ústav teoretické fyziky a astrofyziky

Název práce: Studium mikrokvasarů

Studijní program: Fyzika

Studijní obor: Teoretická fyzika a astrofyzika

Vedoucí práce: Mrg. Filip Hroch, Ph.D.

Akademický rok: 2015/2016

Počet stran: 69

Klíčová slova: mikrokvasar, BHXB, černá díra, akreční disk

Bibliografic Entry

Author: Ondrej Kamenský
Faculty of Science, Masaryk University
Department of Theoretical Physics
and Astrophysics

Title of Thesis: Study of microquasars

Degree Programme: Physics

Field of Study: Theoretical physics and astrophysics

Supervisor: Mrg. Filip Hroch, Ph.D.

Academic Year: 2015/2016

Number of Pages: 69

Keywords: microquasar, BHXB, black hole, accretion disc

Abstrakt

Tato práce má dva cíle. Prvním cílem je poskytnout čtenáři základní informace o mikrokvasarech a o postupech pro zpracování a analýzu dat. Druhým cílem je samotné studium mikrokvasarů GX 339-4 a Cygnus X-1. První kapitoly se zabývají teorií s podporou článků pokrývajících dané téma. Třetí kapitola popisuje získávání a zpracování dat pro jednotlivé rentgenové mise. Poslední kapitoly jsou určeny studiu vybraných objektů, shrnutí výsledků a diskuzi.

Klíčová slova: mikrokvasar, BHXB, černá díra, akreční disk

Abstract

The aim of this work is to provide a reader with basic information on microquasars and on data reduction and analysis procedures. Another aim is a study of microquasars GX 339-4 and Cygnus X-1. First chapters deal with theory referencing most recent articles covering this topic. Chapter three describes data retrieval and reduction processes for individual X-ray missions. The last chapters are dedicated to the study of the microquasars, results summary and a discussion of the results.

Keywords: microquasar, BHXB, black hole, accretion disc



MASARYKOVA UNIVERZITA
Přírodovědecká fakulta

ZADÁNÍ DIPLOMOVÉ PRÁCE

Akademický rok: 2015/2016

Ústav: Ústav teoretické fyziky a astrofyziky

Student: Bc. Ondřej Kamenský

Program: Fyzika

Obor: Teoretická fyzika a astrofyzika

Směr: Astrofyzika

Ředitel Ústavu teoretické fyziky a astrofyziky PřF MU Vám ve smyslu Studijního a zkušebního řádu MU určuje diplomovou práci s názvem:

Název práce: Studium mikrokvasarů

Název práce anglicky: (Study of microquasars)

Oficiální zadání:

Objevem mikrokvasarů se nám dostala do rukou jedinečná astrofyzikální laboratoř ve které máme k dispozici nadsvětelné rychlosti, ale z roků se stávají dny. Přestože se pozorování mikrokvasarů uskutečňuje především v rádiové oblasti, tyto objekty jsou pozorovatelné i ve vysokých energiích. Cílem této práce je experimentální studium vhodně vybraných mikrokvasarů ve vysoko-energieové oblasti. Příkladem může být GRS 1915+105, SS 433 či Sco X-1 pozorované družicí Chandra. K tomu by mělo být použito nejmodernějších astrofyzikálních, statistických metod či metod na zpracování obrazu. Práce by měla obsahovat fyzikální interpretaci výsledků k nimž se dospělo. Práce může být sepsána v jazyce českém, slovenském či anglickém.

Jazyk závěrečné práce: angličtina


Vedoucí práce: Mgr. Filip Hroch, Ph.D.

Datum zadání práce: 3. 2. 2015

V Brně dne: 28. 4. 2016

Souhlasím se zadáním (podpis, datum):


.....
Bc. Ondřej Kamenský
student


.....
Mgr. Filip Hroch, Ph.D.
vedoucí práce


.....
prof. Rikard von Unge, Ph.D.
ředitel Ústavu teoretické fyziky a
astrofyziky

I would like to thank my supervisor for having enough belief in me, that he did not push me and rush me, knowing that I would deliver the thesis in time. I would like to thank him for his advices and remarks. I also would like to thank my girlfriend for her support, for keeping me optimistic and for her understanding in all the times when this work had to be prioritised instead of her.

I declare that I wrote my thesis independently and exclusively with the use of references cited. I agree to lending and publishing of the thesis.

Brno, 10.5.2016

Ondrej Kamenský

Contents

Acronyms	9
Introduction	10
1 Microquasars	11
1.1 Accretion as a source of energy	12
1.2 Known objects and parameters	14
1.2.1 Mass function	15
1.3 Quantitative description	15
1.3.1 X-ray states in spectra	18
1.4 Qualitative description	19
1.4.1 Thermal component	19
1.4.2 Power law component	24
1.4.3 Reflection component	25
1.4.4 Fe-K α line component	25
1.4.5 Absorption component	26
2 Objects of interest	27
2.1 GX 339-4	27
2.2 Cyg X-1	28
3 Detectors	29
3.1 Suzaku	29
3.1.1 Data retrieval	30
3.1.2 Spectrum extraction	30
3.2 XMM Newton	32
3.2.1 Data retrieval	34
3.2.2 Spectrum extraction	34
4 Data retrieval and reduction	36
4.1 GX 339-4	36
4.1.1 XMM Newton	36
4.1.2 Suzaku	37
4.2 Cyg X-1	38

4.2.1	XMM Newton	38
4.2.2	Suzaku	39
5	GX 339-4	40
5.1	Fitting reflection	42
5.2	BHSPEC fitting	44
6	Cyg X-1	49
6.1	Fitting reflection	51
6.2	BHSPEC fitting	53
7	Results	60
8	Discussion	62
	References	63
	Electronic references and sources	67
	Appendix A - Spectrum extraction	68

Acronyms

This is a list of acronyms used in this thesis. They are commonly used in this field of study and should ease the reading of the work.

Acronym	Definition
AGN	Active Galactic Nuclei
BH	Black Hole
BHC	Black Hole Candidate
BHXB	Black Hole X-ray Binary
HID	Hardness Intensity Diagram
HMXB	High Mass X-ray Binary
HR	Hardness Ratio
ISCO	Inner-most Stable Circular Orbit
LMXB	Low Mass X-ray Binary
LOS	Line Of Sight
MBB	MultiBlackBody
MQ	Microquasar
NS	Neutron Star
NSXB	Neutron Star X-ray Binary
PL	Power Law
SPL	Steep Power Law
SSD	Shakura-Sunyaev Disk

Introduction

All history of science provides many examples of astrophysics influencing theoretical physics. The Newton's gravitation and the theory of general relativity are examples. A problem theoretical physics is facing, concerning black hole (BH) physics, is a lack of experiments, a lack of actual BHs somebody can work with. Therefore, astrophysical BHs are the only objects available for testing BH theories. Microquasars (MQs) provide us with a chance to study BH physics, accretion processes, high energy physics and a chance to test other theories otherwise unprovable. Studies of MQs have gone through much development and even though archives are plentiful with data, many of the processes are not properly understood yet. Despite years of research, only a handful of properties and parameters have been determined with such certainty that they are recognised as correct. Unfortunately, most of the results are still just estimates and need to be re-approached, need to be tested in various ways in order to be proven correct. The aim of this work is to present MQs, to describe the variability they undergo, to demonstrate ways of studying them and to test some of the recent results or to bring new ones.

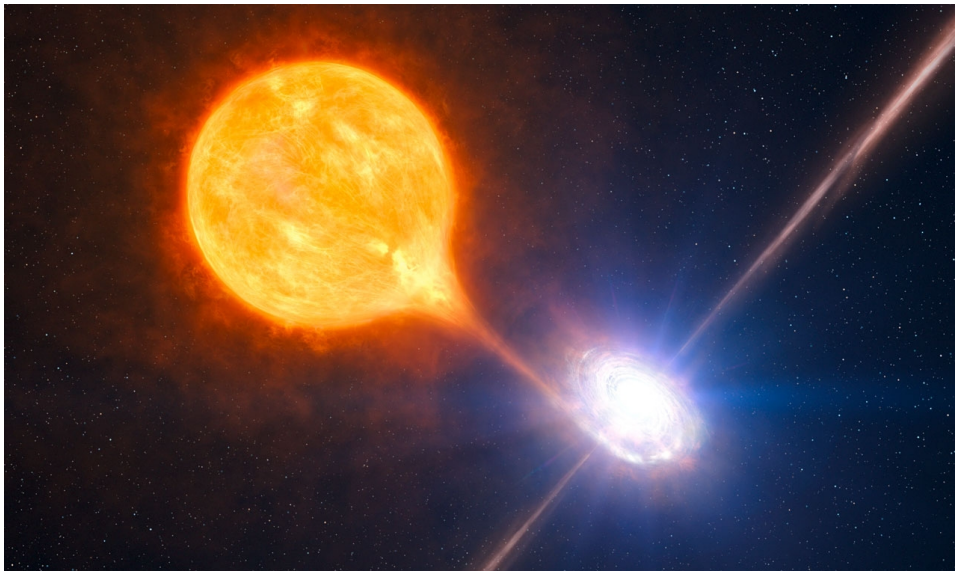


Figure 2: A microquasar – an artist's impression [e1]

Microquasars

„What the hell is a (micro)quasar?“

(Arnold J. Rimmer)

A (MQ) is a label for a black hole X-ray binary (BHXB). The first object to be referred to as MQ is 1E170.7-2942 due to a double sided jet detected coming from it. It was mimicking jets of a quasar, just on smaller scales. Therefore the name. Next objects to be called MQs were, for example, GRS1915+105 and SS433. However, not all BHXBs were labelled as MQs. The condition was the detection of relativistic jets with bulk motion speed over 90 % of the speed of light. This nicely ruled out neutron star X-ray binaries (NSXBs), whose bulk motion speeds were measured to be below 50 % of the speed of light. However, a discovery of highly relativistic jet bursting from a NSXB broke the labelling rule. The jets lost their role in determining a MQ.

Despite the scale difference between actual quasars and MQs, the processes driving the activity of both classes might be quite similar. Of course the size difference is related to the temporal variability and therefore jets are a reoccurring feature of a BHXB. This fact offers an idea that different kinds of quasars might not be caused just by the point of view from which we observe the object. The reasons for different behaviour might be more complicated, like different morphology of the central surroundings or even state transitions on a very long time scale. Therefore, the terms BHXB and MQ become equal and shall be used interchangeably in the rest of the work.

A MQ system consists of two main components, a donor star and a compact object. The matter flowing from the donor star does not fall directly onto the compact object, but creates an accretion disc due to conservation of angular momentum. Other components are, for example, a corona as a source of high energy radiation and double-sided jets emitting radio radiation. The research of these objects is closely connected to the development of the observational technology. New missions bring new data, better than before. This kind of objects can be studied across a wide range of energies. Jets in radio wavelengths, companion star in visible light (only limited amount of cases) but most of all in higher energies, in X-ray wavelengths. This thesis is focused on observing the X-ray radiation detected with X-ray spacecrafts orbiting Earth.

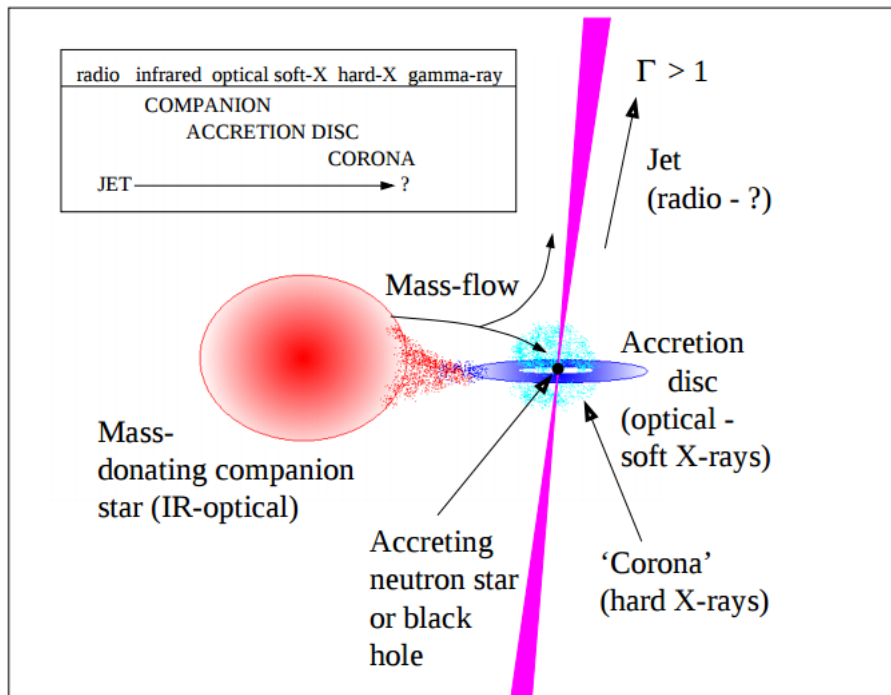


Figure 1.1: A description of the components of a MQ system (Fender, 2002)

1.1 Accretion as a source of energy

We will consider the amount of energy extracted from nuclear fusion reactions. The highest efficiency is reached in the case of hydrogen atoms being merged into helium, which is also the most common case of such a reaction in stars. The amount of energy is

$$\Delta E = 0.007mc^2, \quad (1.1)$$

where m stands for the mass of the hydrogen entering the reaction and c is the speed of light (Frank et al., 2002). This process extracts $\sim 4 \times 10^{30}$ keV.kg $^{-1}$. To compare nuclear fusion to accretion, we will set a simple approximation of spherically symmetric inward fall of material onto a compact object. The extracted gravitational energy will be

$$\Delta E = \frac{GM_*m}{R_*}. \quad (1.2)$$

In the case of an accreting neutron star with radius $R_* \sim 10$ km and $M_* \sim M_\odot$ the efficiency results in $\sim 6 \times 10^{31}$ keV.kg $^{-1}$, being about 15 times higher than in the case of nuclear hydrogen burning. Nevertheless, this efficiency is a function of “compactness” of the central object. As the ratio M_*/R_* gets higher, the efficiency gets higher as well.

However, this is a rather simple approximation of matter falling directly inwards. In reality, the matter is carrying non-zero angular momentum, which results in accretion. The matter is accumulated in an accretion disk, following Keplerian velocity distribution, $v(r) \propto r^{-1/2}$. This means that neighbouring areas of the matter have different orbital velocities and slide past one another which, thanks to viscosity, creates shearing. This process helps to transfer angular momentum outwards.

The inner parts of the disc moving with higher velocity need to eliminate the angular momentum in order to fall closer to the centre. This is achieved by shearing, when friction between two neighbouring areas allow for the angular momentum to be transferred. The efficiency of redistributing of the angular momentum depends on the viscosity of the material.

When falling inwards, part of the potential energy is transferred into kinetic energy. Another part is transferred into internal energy and heats up the matter. As the matter gets closer to the centre, the temperature rises. This results in strong thermal electromagnetic radiation from the disc itself. For a typical BHXB, the inner temperature of the disc rises up to $\sim 10^7$ K, with the maximum of the radiation around X-ray wavelengths ~ 0.25 nm. This emission plays an important role in studying MQs. (See Section 1.4.1)

Another important effect originating in the accretion process is the Eddington limit. The mechanism of accretion brings the material closer and thus delivers fuel. However, outgoing radiation produces pressure upon the incoming material. As more material is delivered closer to the center, the luminosity rises and so does the radiation pressure. At a certain point, the radiation pressure may get so high that it actually stops the inward flow of the accreted material. This process results in the loss of fuel and luminosity decreases, along with the radiation pressure. Therefore, these objects cannot have higher luminosity than the Eddington limit for a long time and if they ever reach the limit, they tend to fluctuate around it. To determine the limit, we will set the radiation force equal to the gravitational force:

$$F_L \equiv \frac{L\sigma_T}{4\pi r^2 c} = F_g \equiv \frac{GMm}{r^2}, \quad (1.3)$$

where L is the luminosity, σ_T is the Thomson cross section, which is dependent on the material and m is the mass of the accreted particle. We can now express L for the case of fully ionized hydrogen with the mass of the central object expressed in solar masses:

$$L_{\text{Edd}} = \frac{4\pi cGMm}{\sigma_T} = 1.26 \times 10^{31} \left(\frac{M}{M_\odot} \right) W. \quad (1.4)$$

The accreted matter can be supplied from the companion star in two ways. In order to be trapped by the gravitational pull of the compact object the matter has to leave the vicinity of the donor star, where it still “belongs” to the donor star. This is done either by a stellar wind or by the Roche lobe overflow. The former situation is

less important, as stellar winds do not continuously supply a lot of matter to the disc. However, at some point of the evolution, a massive ejection of the mass might occur. The latter situation is either a result of the evolution of the star or a result of a change in the binary orbital parameter. When momentum is lost (e.g. due to mass loss by stellar winds) the binary separation shrinks and the Roche lobe radius is lowered. Most common cause of a star filling its Roche lobe is the stellar evolution. The donor star can, in later phases of its evolution, blow away its upper atmosphere into higher radii. At this point, the matter is moved from one gravitational well to that of the compact object where it is accumulated in the accretion disc. In the case of a high mass overflow the stream can be a distinctive part of the system. It can, for example, cross the line of sight in short-period binaries and create variable absorption.

1.2 Known objects and parameters

Table 1 provides a summary of MQs and their parameters taken from (Zhang, 2013), combined with the spectral types of donor stars listed in the original table from (Remillard and McClintock, 2006).

Coordinate Name	Common Name/Prefix	P_{orb} (hr)	$f(M)$ (M_{\odot})	M_{BH} (M_{\odot})	Spec. type (Donor)	a_* (cJ/GM^2)
0422+32	(GRO J)	5.1	1.19 ± 0.02	3.7–5.0	M2V	–
0620-003	(A)	7.8	2.72 ± 0.06	6.35–6.85	K4V	0.12 ± 0.19
1009-45	(GRS)	6.8	3.17 ± 0.12	3.6–4.7	K7/M0V	–
1118+408	(XTE J)	4.1	6.10 ± 0.30	6.5–7.2	K5/M0V	–
1124-684	Nova Mus 91	10.4	3.01 ± 0.15	6.5–8.2	K3/K5V	–
1354-64	(GS)	61.1	5.75 ± 0.30	–	GIV	–
1543-475	4U	26.8	0.25 ± 0.01	8.4–10.4	A2V	0.75–0.85
1550-564	(XTE J)	37.0	6.86 ± 0.71	8.4–10.8	G8/K8IV	0.06–0.54
1650-500	(XTE J)	7.7	2.73 ± 0.56	–	K4V	–
1655-40	(GRO J)	62.9	2.73 ± 0.09	6.0–6.6	F3/F5IV	0.65–0.75
1659-487	GX 339-4	42.1	5.80 ± 0.50	–	–	–
1705-250	Nova Oph 77	12.5	4.86 ± 0.13	5.6–8.3	K3/7V	–
1743-322	(H)	–	–	–	–	0.20 ± 0.30
1819.3-2525	V4641 Sgr	67.6	3.13 ± 0.13	6.8–7.4	B9III	–
1859+226	(XTE J)	9.2	7.40 ± 1.10	7.6–12.0	–	–
1915+105	(GRS)	804.0	9.80 ± 3.00	10.0–18.0	K/MIII	0.98–1.0
1956+350	Cyg X-1	134.4	0.244 ± 0.005	13.8–15.8	O9.7Iab	> 0.95
2000+251	(GS)	8.3	5.01 ± 0.12	7.1–7.8	K3/K7V	–
2023+338	V404 Cyg	155.3	6.08 ± 0.06	10.0–13.4	K0III	–
0538-641	LMC X-3	40.9	2.3 ± 0.3	5.9–9.2	B3V	< 0.3
0540-697	LMX X-1	93.8	0.13 ± 0.05	9.4–12.5	O7III	0.94–0.99
0020+593	IC 10 X-1	34.9	7.64 ± 1.26	> 20	–	–
0055-377	NGC 300 X-1	32.3	2.6 ± 0.3	> 10	–	–
0133+305	M33 X-7	82.9	0.46 ± 0.07	14.2–17.1	–	0.84 ± 0.05

Table 1.1: Table of known MQs (Remillard and McClintock, 2006; Zhang, 2013)

1.2.1 Mass function

The values in the fourth column are the best estimates for the lower mass limit of the compact object. These results come from dynamical studies and therefore are most reliable for the mass estimation. The final formula (1.9) is derived from the third Kepler law (1.5). Given that $q \equiv M_2/M_1$, the total mass of the system can be transformed (1.6) along with the major semiaxis (1.7). The inclination is denoted as i . The major key of this procedure is the measurement of the orbital period P_{orb} and the radial velocity amplitude K_2 of the donor star.

$$GM = \left(\frac{2\pi}{P_{\text{orb}}} \right)^2 a^3, \quad (1.5)$$

$$M = M_1 + M_2 = M_1 \left(1 + \frac{M_2}{M_1} \right) = M_1(1 + q), \quad (1.6)$$

$$a^3 = (a_1 + a_2)^3 = a_2^3(1 + q)^3, \quad (1.7)$$

$$P_{\text{orb}} = \frac{2\pi}{\omega} = \frac{2\pi a_2}{v_2} = \frac{2\pi a_2 \sin(i)}{K_2}. \quad (1.8)$$

All these combined give the following mass function $f(M)$ (1.9). If the orbital period and the radial velocity amplitude are measured, the mass function gives a lower mass limit of the compact source. The maximum value of $\sin i$ is 1 and the minimal value of q is 0, making the $f(M)$ the lower boundary for M_1 . Measuring the mass function is a strong proof for deciding on whether a BHC is a true BH.

$$f(M) \equiv \frac{P_{\text{orb}} K_2^3}{2\pi G} = \frac{M_1 \sin^3(i)}{(1 + q)^2} \quad (1.9)$$

1.3 Quantitative description

A discrete classification of this kind of objects is very difficult. Although significant results have been achieved for describing evolution tracks of BHXBs, different objects usually resemble each other only in basic traits due to different conditions. A very good, yet not absolutely complete tool, is a hardness intensity diagram (HID). The HID is an equivalent of the Hertzsprung-Russel diagram for evolution tracking. However, the evolution in this case is in a form of a loop. The diagram depicts the source intensity versus the hardness ratio (HR), computed as the ratio of count rates in two energy bands. The big advantage of the HID is that it is model independent. An example of this diagram is shown in Figure 1.2.

We will set the right-bottom corner of the HID as the starting point of the evolution loop. This area of the “q-shaped” diagram is referred to as the **quiescent state**. MQs tend to spend most of their lifetime in this state with low luminosity, high HR and very little variability. However, there are exceptions when a MQ does not fall into the quiescent state and rather immediately repeats the cycle.

One example of such behaviour is the GX 339-4 MQ, which has been very active since its discovery. On the other hand, the GRS1915+105 truly stays most of the time (even years) in the calm, invariable quiescent state. Most of all, MQs are never discovered while in this state due to very faint luminosity. They are mostly discovered in the moment of an outburst and only then they can be tracked returning into this stop of the cycle. In this state, the inner regions of the disc are truncated, there is a sparse corona responsible for a weak hard X-ray component. Radio jets are weak and present rather randomly. The low luminosity of this state is important for dynamical observations, as the spectrum of the donor star can get prominent and allow the measurement of orbit velocities.

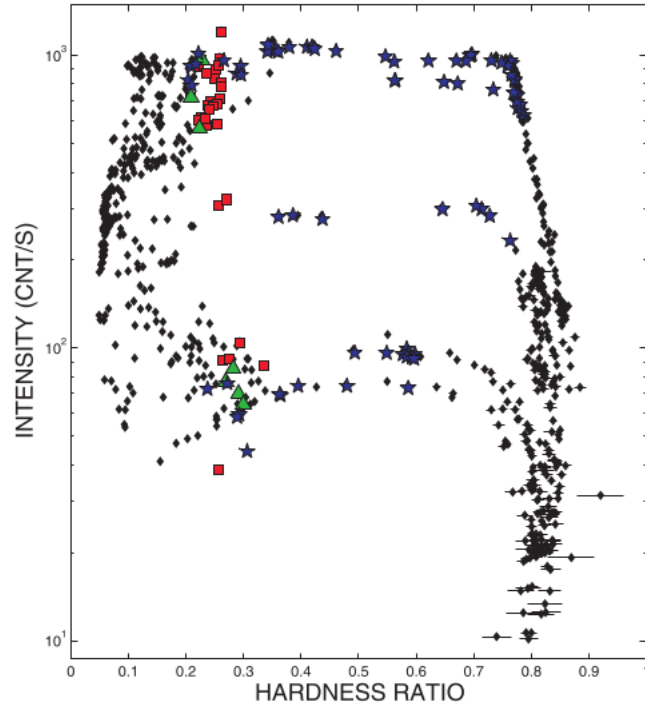


Figure 1.2: Hardness Intensity Diagram (Motta et al., 2011)

In the case of an outburst the luminosity rises severely, with the HR remaining high. Previously random and weak jets are now strong and permanent. This vertical rise of the MQ is referred to as the **hard state**. At this point, the soft spectral component is weak or even absent and a massive corona is formed, which results in a very strong hard power law component (PL) of the spectrum. The photon index Γ of the PL is close to 1.7 and these spectra usually suffer from an exponential cutoff near 100 keV. In addition, part of the hard X-ray radiation is scattered towards the disc and reflected from it. Depending on the inclination of the disc in respect to the observer a reflection component occurs along with possible occurrence of the emission iron line feature.

The following state is the **steep power law state** (SPL). While in the hard state the photon index was $\Gamma \sim 1.7$, it rises above 2.4 in the SPL state. This state is situated in the top left half of the HID. The inner regions of the disc are no more truncated and the soft X-ray component of the spectrum is cognizable. Nonetheless, strong corona is still present and the hard X-ray component does not suffer from the cutoff and extends up to \sim MeV. Jets are present only till a certain breakpoint. When moving from right to left, the jet outburst may get violent when the MQ is passing the middle section and disappear as the MQ gets closer to the left edge of the HID.

If we consider a simple case when the MQ undergoing an outburst directly follows the q-shaped loop, the MQ goes from the SPL state to the **thermal** (or soft) state. This state has a distinctive thermal component described as \sim 1 keV and a faint variable PL component. The weak PL component is due to absent or very sparse corona and jets are not observed. As a result of the absence of a strong PL component, the reflection component tends to be absent as well.

As stated at the beginning of the section, the previous discrete classification is not complete. There are numerous **intermediate** states, when a MQ transfers from one state to the next one and shares features of both states. Especially the transit between the hard and the SPL state is very important as it correlates to the changes in the radio emissions and the restoration of the inner disc regions.

The truncation and refilling of the inner regions of the accretion disc are connected to the spin parameter of the central BH. The spin is defined as a unitless value $a_* \equiv cJ/GM^2$, where J is the angular momentum of the BH. The spin determines the innermost stable circular orbit (ISCO) of the disc. For non-rotating Schwarzschild BHs with $a_* = 0$ the ISCO lies at $6 r_g$. The opposite situation is a maximally rotating Kerr BH, with $a_* = 1$, when the ISCO stretches down to $1 r_g$. (Remillard and McClintock, 2006) The gravitational radius is defined as $r_g \equiv GM/c^2$.

State name	Features of X-ray state
Thermal	Disk fraction $f^a > 75$ % $T_{\text{in}} \sim 1$ keV jets absent
Hard	$f^a < 20$ % $1.4 < \Gamma < 2.1$ jets present ~ 100 keV cutoff
Steep Power Law (SPL)	$\Gamma > 2.4$ $f^a < 50$ % - 80 % jets violent or absent PL up to \sim MeV

Table 1.2: Summary of the features of the MQ states. a is taken from (Remillard and McClintock, 2006).

1.3.1 X-ray states in spectra

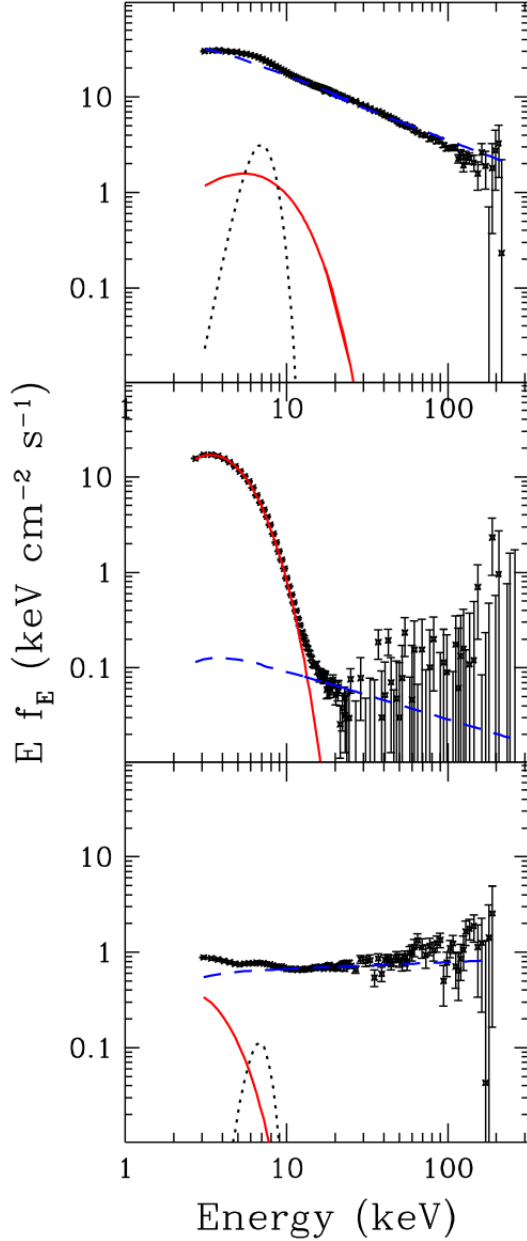


Figure 1.3: X-ray states of a MQ (Remillard and McClintock, 2006)

These spectra of GRO J1655-40 taken from (Remillard and McClintock, 2006) are examples of SPL state, thermal state and hard state respectively. They present energy distribution decomposed into three components: red solid line for thermal, blue dashed for power law and black dotted for relativistically broadened Fe $K\alpha$ line. All three observations were carried out by RXTE.

The first spectrum (Aug 1st 1996) is a typical SPL state. There is a cognizable thermal component, alongside with steep PL. There is also a distinctive iron line feature originating in reflection on the accretion disc. As the inner parts of the disc are not truncated, the relativistic effects upon the iron line are very prominent, making it very wide.

The second spectrum (Mar 24th 1997) consist of a weak PL component and a very strong thermal component. Since there is very little reflected radiation, the iron line is absent.

The last spectrum (Aug 14th 1997) is the opposite of the previous spectrum. The thermal component is weak and a strong PL component is present, along with the iron line. It is also noticeable that intensity in the hard state is approximately 10 times lower than in the thermal state.

1.4 Qualitative description

This section deals with the spectral components separately. It describes processes that generate and shape particular components, mainly the thermal component that originates in the accretion disc itself. Most of all, it presents commonly used XSPEC (Arnaud, 1996) models designed for each of the components, describes their parameters and in some cases compares different XSPEC models.

1.4.1 Thermal component

Thin disc prescription

A thin disk model is an approximation neglecting the thickness of the disc in the cylindrical coordinate system. It provides reasonable results for cases when $H \ll R$, where H is the horizontal thickness of the disc. Fortunately, this condition is often met. One example of such model is the Sakura-Sunyaev (SSD) thin disc solution (Frank et al., 2002). The model includes a unitless parameter α , which represents a certain law of viscosity of the accreted material as $\nu = \alpha c_s H$ where c_s is the sound velocity. This parameter is usually given beforehand to be 0.1 or 0.01 and is almost never estimated by fitting. These equations were taken from (Frank et al., 2002) (expressed in cgs system) and describe some of the disc parameters:

$$\Sigma = \rho H, \quad (1.10)$$

$$T_c = 1.4 \times 10^4 \alpha^{-1/5} \dot{M}_{16}^{3/10} m_1^{1/4} R_{10}^{-3/4} f^{5/6} \text{K}, \quad (1.11)$$

$$\Sigma = 5.2 \times \alpha^{-4/5} \dot{M}_{10}^{7/10} m_1^{1/4} R_{10}^{-3/4} f^{14/5} \text{g.cm}^{-2}, \quad (1.12)$$

$$H = 1.7 \times 10^8 \alpha^{-1/10} \dot{M}_{16}^{3/20} m_1^{-3/8} R_{10}^{9/8} f^{3/5} \text{cm}, \quad (1.13)$$

$$\nu = 1.8 \times 10^{14} \alpha^{4/5} \dot{M}_{16}^{3/10} m_1^{-1/4} R_{10}^{3/4} f^{6/5} \text{cm}^2 \cdot \text{s}^{-1}, \quad (1.14)$$

$$v_R = 2.7 \times 10^4 \alpha^{4/5} \dot{M}_{16}^{3/10} m_1^{-1/4} R_{10}^{-1/4} f^{-14/5} \text{cm.s}^{-1}, \quad (1.15)$$

$$f = \left[1 - \left(\frac{R_*}{R} \right)^{1/2} \right]^{1/4}, \quad (1.16)$$

where input variables are expressed in terms of $R_{10} = R/(10^{10} \text{ cm})$, $m_1 = M/M_\odot$, $\dot{M}_{16} = \dot{M}/(10^{16} \text{ g.s}^{-1})$ and R_* stands for the radius of the central object. These units are modified to closely fit parameters of a white dwarf. The temperature profile for the case of an ordinary MQ is presented in Figure 1.4, the parameters are stated in the caption and the x axis is expressed in r_g . The profile nicely follows the presumption of the truncation of the inner regions of the disc explained in Section 1.3. At bigger distances from the center, the temperature decreases rapidly. That results in a very weak presence of the thermal component of the spectrum, or rather in low temperature of the thermal component. Figure 1.5 shows the height of the disc H with respect to R also with the ratio H/R . (Input parameters same as in Figure 1.4)

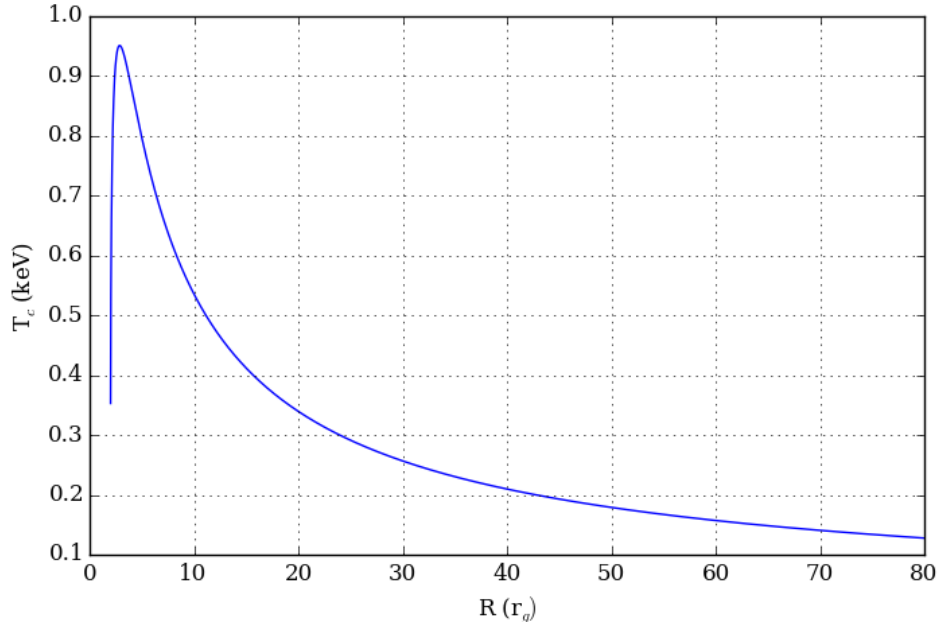


Figure 1.4: SSD temperature profile ($M = 15.0 M_{\odot}$, $\alpha = 0.1$, $\dot{M} = 10^{-6} M_{\odot} \cdot \text{y}^{-1}$)

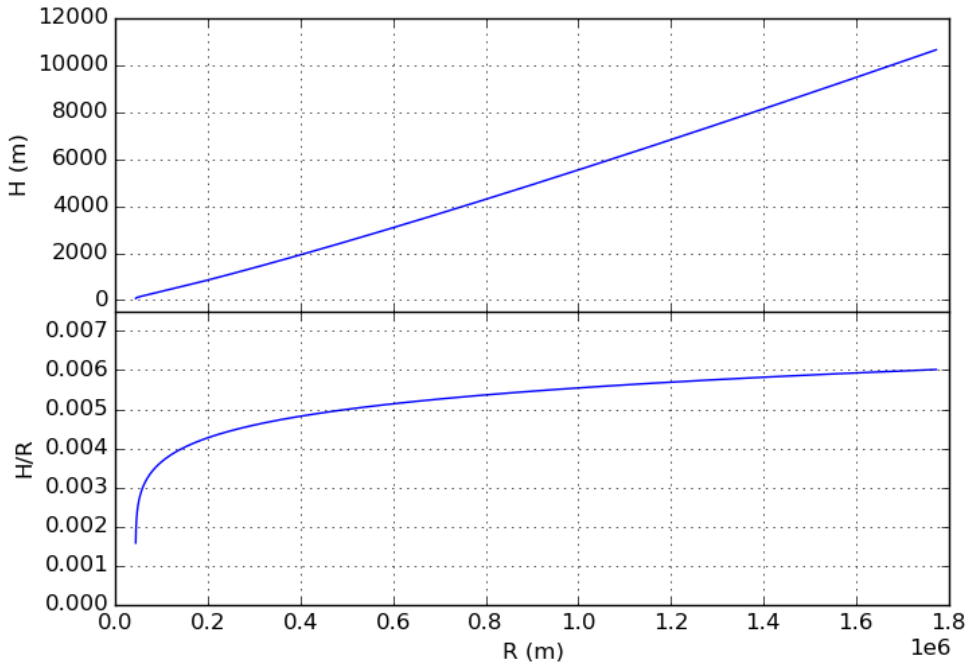


Figure 1.5: Height of the disc H and ratio H/R as functions of radius R .

Multi blackbody

Describing radiation from a disc with a temperature profile as shown in Figure 1.4 by a simple blackbody model would be incorrect, since there is no constant temperature. However, there is a distinctive “inner” temperature, the highest temperature at the inner boundary. The rest of the profile follows a rather simple function close to $\sim R^{-3/4}$. The overall spectrum can thus be described as a multi-blackbody spectrum (MBB). This spectrum can be acquired by integrating multiple blackbody distributions over the disc temperature profile:

$$\begin{aligned}
 f(E) &= \frac{\cos \theta}{D^2} \int_{r_{\text{in}}}^{r_{\text{out}}} 2\pi r B(E, T) dr = \\
 &= \frac{8\pi r_{\text{in}}^2 \cos \theta}{3D^2} \int_{T_{\text{out}}}^{T_{\text{in}}} \left(\frac{T}{T_{\text{in}}} \right)^{-11/3} B(E, T) \frac{dT}{T_{\text{in}}},
 \end{aligned} \tag{1.17}$$

where D stands for distance, θ stands for disc inclination, $T_{\text{in}} = T(r_{\text{in}})$ is the highest temperature at the inner edge of the disc and $B(E, T)$ represents the Planck blackbody distribution. (Mitsuda et al., 1984) The result of this simple MBB model is presented in Figure 1.6, using the temperature profile in Figure 1.4. As well as stars cannot be precisely described as black bodies, describing an accretion disc by a multi black body profile is not entirely correct. Nonetheless, it provides a rather accurate estimate.

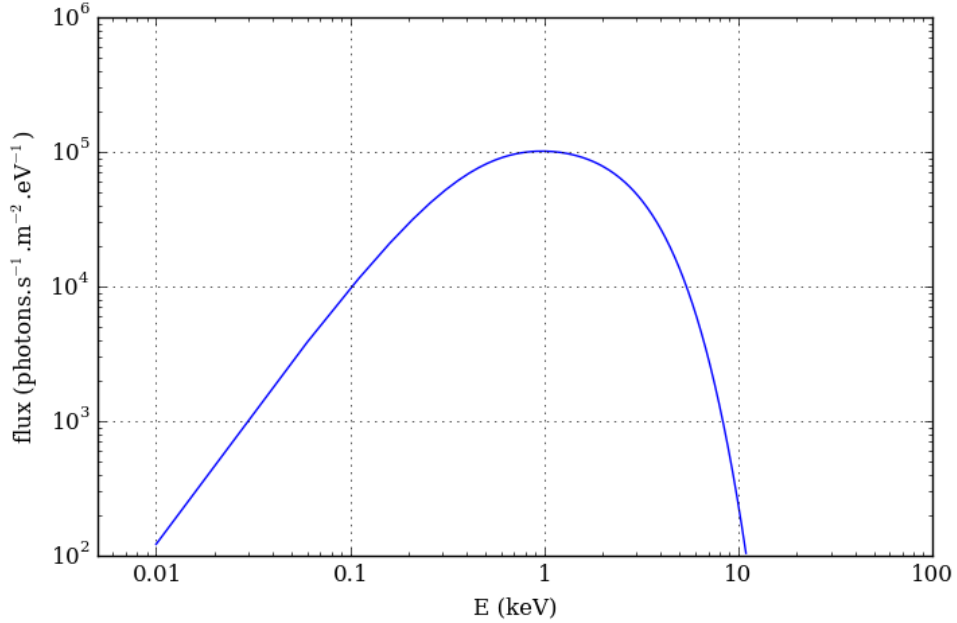


Figure 1.6: MBB profile, result of Equation (1.17) applied to Figure 1.4

DISKBB and BHSPEC

DISKBB is a basic model in XSPEC and represents a simple MBB model similar to SSD. It has two input parameters, T_{in} and $norm$. T_{in} is the inner temperature and corresponds to the temperature in (1.17). The parameter $norm$ represents

$$\left[\frac{(R_{\text{in}}/\text{km})}{(D/10\text{kpc})} \right]^2 \cos \theta, \quad (1.18)$$

where R_{in} is the inner disc radius, D is the distance and θ is the disc inclination. An example of DISKBB is included in Figure 1.7, where the shape of the thermal component resembles the profile in Figure 1.6 rather well.

BHSPEC computes the thermal spectrum of an accretion disc with respect to relativistic effects (Davis et al., 2005). It uses models of stellar atmospheres to calculate the radiation from disc annuli. The model is in a tabular form and user has to choose a particular table based for example on the α parameter. The relativistic effects are mentioned in the paragraph about the iron line component.

The input parameters of the BHSPEC are the logarithmic mass of the compact object $\log(M/M_{\odot})$, the logarithmic luminosity of the MQ as a fraction of the Eddington luminosity $\log(L/L_{\text{edd}})$, the cosine of the inclination of the disc $\cos i$, the unitless spin parameter of the compact object a_* and the normalisation parameter $norm = (10\text{kpc}/D)^2$, where D stands for distance.

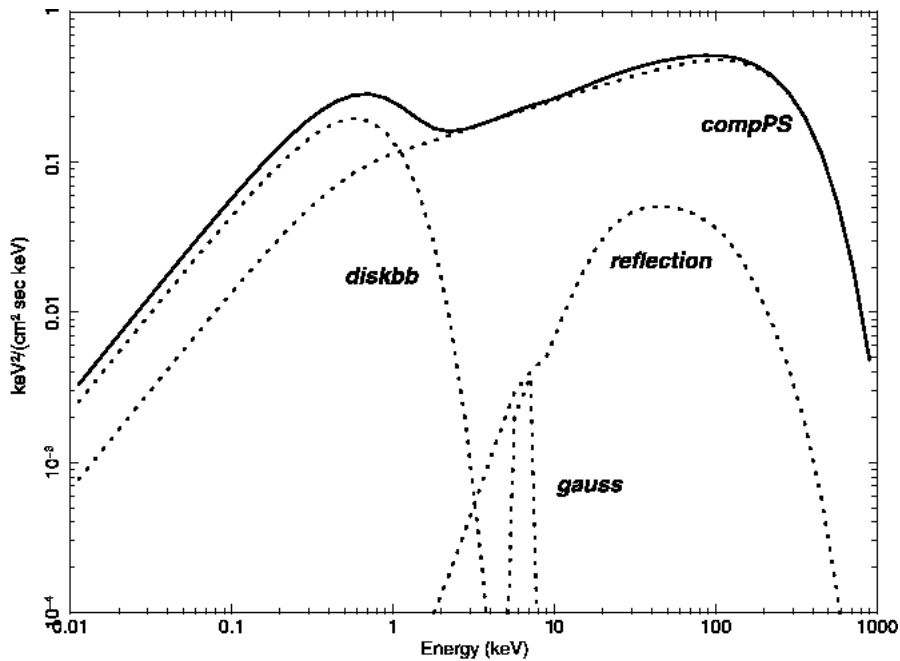


Figure 1.7: BHBX modelled spectrum components (Paizis et al., 2009)

Figure 1.8 compares the two XSPEC models BHSPEC and DISKBB. First, simulated data were generated using models `wabs*bhspec`. The model WABS represents interstellar absorption and is dealt with in Section 1.4.5. The input parameters were $nH = 0.526$, $\log(M/M_\odot) = 1.14$, $\log(L/L_{\text{edd}}) = -1.04$, $\cos i = 0.7$, $a_* = 0.98$, $norm = 9.0$ and data were generated using response matrices of PN instrument of XMM Newton from the observation number 0148220201 (GX 339-4). Afterwards, the simulated data were fitted with `wabs*diskbb` in order to demonstrate the differences. The resulting parameters of the DISKBB model were $T_{\text{in}} = 0.876$ keV and $norm = 9228.61$.

If the K and $\cos i$ parameters are inserted into the DISKBB's $norm$ parameter, the inner radius results in $R_{\text{in}} \approx 38$ km. As a_* approaches 1, the ISCO falls down to $1 r_g$. In this situation the spin parameter was fixed at near maximum value $a_* = 0.98$ and R_{in} is above the r_g which is ~ 20.5 km.

The bottom part of Figure 1.8 contains ratio between the simulated data and the model. Even though the differences might seem sufficiently large, the probability of them being detected depends on the quality of the studied data. The choice which model to use should be affected by presumption of the inner radius. When the inner regions of the disc are truncated, the relativistic effects are not very prominent and a simple model is sufficient. However, when considering SPL or Thermal state, the disc extends down to low radii and the relativistic effects may strongly influence the radiation.

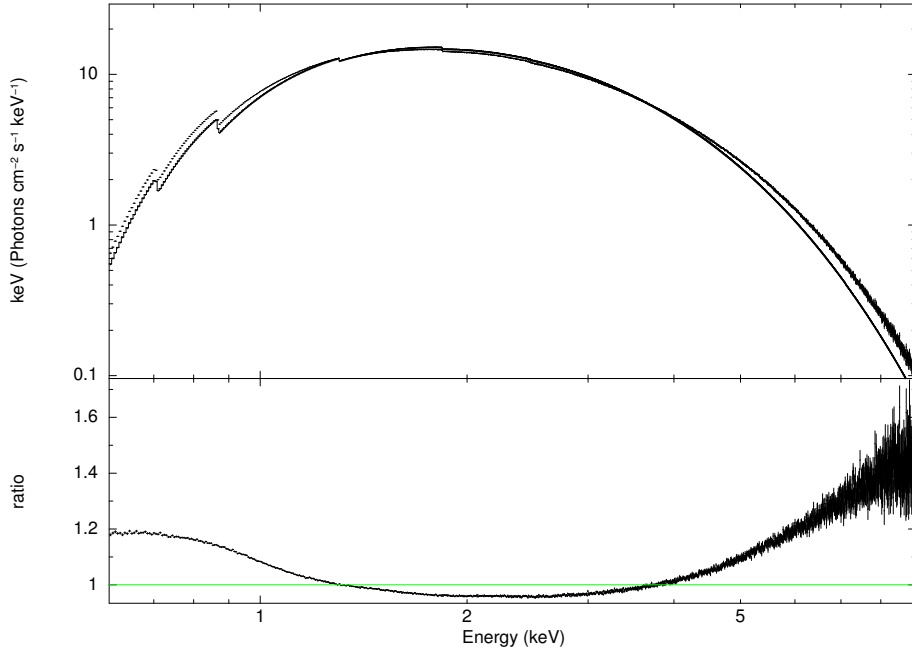


Figure 1.8: DISKBB applied to simulated BHSPEC data and model to data ratio

1.4.2 Power law component

This component is expressed by a quite simple formula (1.19) but the mechanism behind this high energy radiation is still a bit unclear. The mostly accepted theory uses inverse Compton scattering to produce the non-thermal radiation.

$$A(E) = K.E^{-\Gamma} \quad (1.19)$$

The scattering is thought to occur in a corona, consisting of very hot electrons. The corona is created by evaporation of the accreted material in the inner regions of the disc. Thermal photons coming from the disc are scattered up by the electrons to higher energies. While the disc occupies regions outside r_{in} , the corona is located between r_{in} and ISCO. In the hard state $r_{\text{in}} \gg \text{ISCO}$ and thus the disc emission is poor and sometimes hardly detectable. Otherwise, in the soft state $r_{\text{in}} \rightarrow \text{ISCO}$ and the corona is absent while the disc dominates the spectrum.

In XSPEC, two basic models represent this spectral component, POWERLAW and BKNPOWER. The POWERLAW model has two input parameters, the photon index Γ and the multiplication factor K (photons $\text{keV}^{-1}\text{cm}^{-2}\text{s}^{-1}$ at 1 keV). An example of POWERLAW is contained in Figure 1.9 (red dotted line). The BKNPOWER model has a broken power law profile. It has four parameters: two photon indexes Γ_1 and Γ_2 , normalisation K parameter and a break point for the energy E_{break} . The broken power law model is applicable to a spectrum that suffers from inconsistency, for example in the case of inconsistent temperature profile.

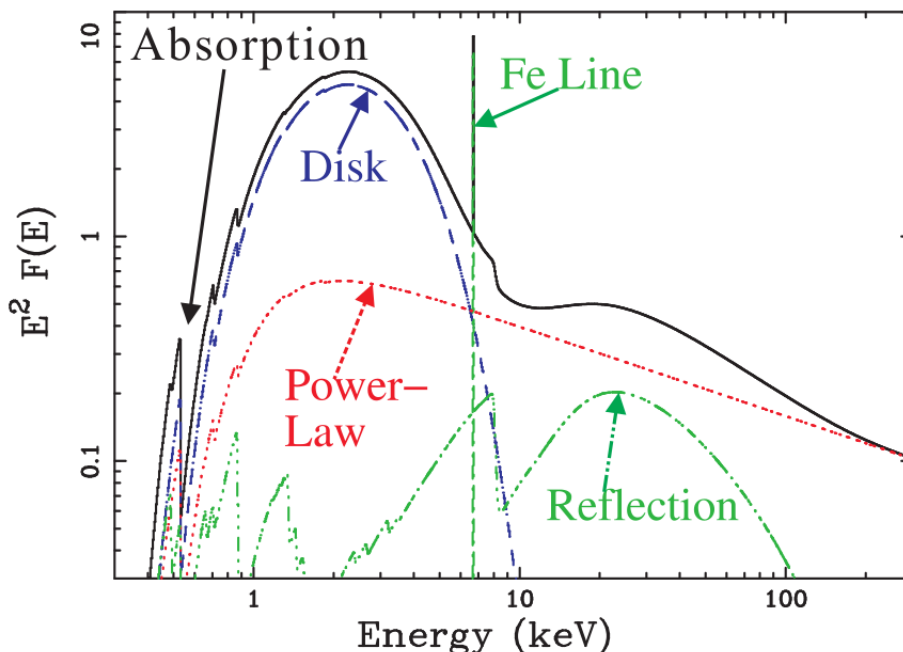


Figure 1.9: Spectral components (Adapted from Figure 3b from (Miller, 2007))

1.4.3 Reflection component

A typical feature of this component is a Comptonian hump with a maximum at ~ 20 keV and an emission Fe $K\alpha$ line as seen in Figure 1.9 (green dashed line). The reflection models use an ordinary power law distribution of radiation to simulate the reflected spectrum. Most models work with an optically-thick disc and solve radiative transfer equations to obtain the outgoing radiation. As for the XSPEC models, this work uses RELXILL model (García et al., 2013), which is a result of merging XILLVER (continuum reflection), RELLINE (relativistically broadened emission lines) and RELCONV (relativistic smearing of the whole spectrum).

The RELXILL model is a table model with 15 parameters, of which many are frozen by default. To name a few of the parameters, the model fits for the iron abundance of the disc, the ionization parameter χ_i , the photon index of the power law illumination Γ , r_{in} , r_{out} , inclination, spin of the BH and more.

1.4.4 Fe- $K\alpha$ line component

The reflection of high energy radiation on the accretion disc results in occurrence of a fluorescent iron $K\alpha$ line at 6.4 keV. This spectral component is very important because it allows probing the inner parts of the disc without the need of knowing the exact distance of an object in contrary with the continuum fitting method. The relativistic effects acting upon the line profile are dependent for example on the radius and thus the line can be used to derive the r_{in} parameter and to estimate the spin of a BH.

The relativistic effects are presented in Figure 1.10. A simple emission line is thermally broadened and then two effects are applied: gravitational redshift (1.20) and relativistic boosting (1.21). The redshift was taken and simplified from (Bao et al., 1994). Figure 1.10 shows the asymmetric line broadening for different inclination angles.

$$z = \left(\frac{r}{r-3}\right)^{1/2} + \left(\frac{r}{(r-2)(r-3)}\right)^{1/2} \sin i \frac{\sin \phi_s}{\sqrt{1 - \cos^2 \phi_s \sin^2 i}} - 1, \quad (1.20)$$

$$I = \left(\frac{\omega}{\omega_0}\right)^3 I_0. \quad (1.21)$$

In (1.20) r stands for the radius of currently processed segment, ϕ_s is its azimuth (the observer is at $\phi_s = 0$) and i is the system inclination. In the process of creating the spectrum in Figure 1.10, the disc was divided into a set of annuli divided into angular segments. An emission line was calculated for each segment and thermal Doppler broadening was used. (temperature and density derived from parameters in Figure 1.4) Then for each segment, both relativistic effects were applied. The result is of course just a rough example, supposed to present the relativistic effects. It does not include variable disc emissivity or any iron abundance profile.

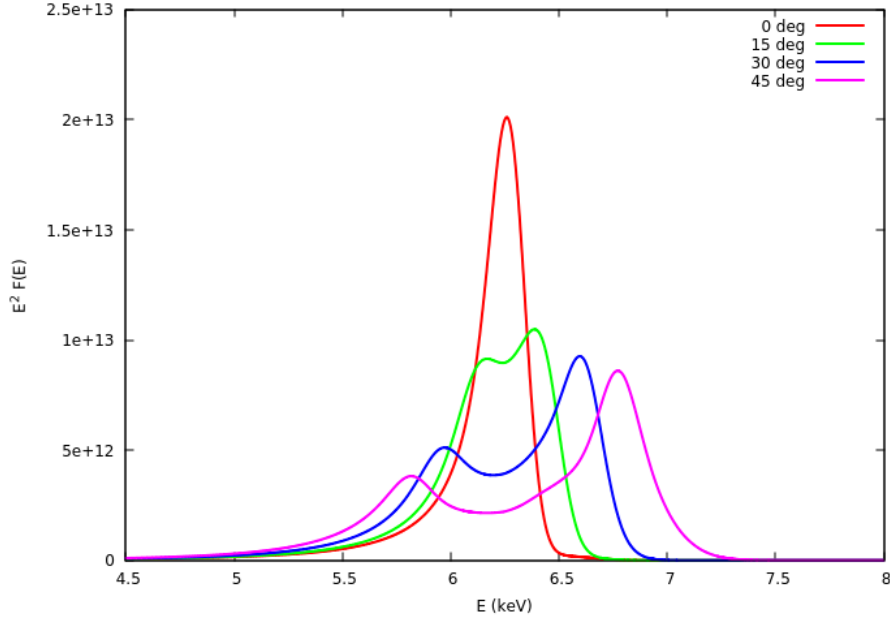


Figure 1.10: Relativistic broadening of an emission line

In XSPEC, the Fe $K\alpha$ line is included in some reflection models, but can be applied separately. The models are LAOR and KYRLINE. Description and comparison of these two models can be found in (Svoboda et al., 2009).

1.4.5 Absorption component

The contribution to this process can be split between two sources, the interstellar absorption and the absorption occurring within the MQ. The former tends to remain constant, while the latter tends to change. As for X-ray radiation, absorption affects mostly soft X-rays (thermal component) and should never be omitted from the fitting procedure. In XSPEC, there are many default models for the absorption, e.g. WABS, PHABS, TBABS, etc. Differences between models are caused by what processes the model takes into account. A physical parameter all of them share is the hydrogen column density nH (10^{22} atoms/cm²). As for X-ray wavelengths the absorption is not at all dominated by hydrogen atoms, but by heavier elements. Their relative abundances are expressed by the hydrogen column.

When working with X-ray spectra, it is advisable to set boundaries of the nH parameter. These boundaries can be looked for in other articles concerning the objects of interest or derived from HI surveys from the area. And while the interstellar component is usually constant, the other component may vary on different scales. The MQ Cyg X-1, for example, has been reported to show strong nH variability over its 5.6 days binary orbit period. (Grinberg et al., 2015)

Objects of interest

2.1 GX 339-4

This MQ was discovered in 1973 (Markert et al., 1973) and is classified as a Low Mass X-ray Binary. The low mass definition describes the companion star, whose mass is comparable to the mass of the Sun. It is located in the constellation Ara at coordinates $\alpha = 17^{\circ}02'49.36''$ and $\delta = -48^{\circ}47'22.8''$. Due to the fact that GX 339-4 is very active and has undergone many outbursts the spectral class of the companion star is uncertain. GX 339-4 does not fall into the quiescent state and rather tends to repeat the outburst cycle without its brightness lowering very much. An important point in the research of this object is the determination of the mass function with dynamical methods from spectroscopic data (Hynes et al., 2003). The mass function explained in Section 1.2 is in the case of GX 339-4 estimated to be $(5.8 \pm 0.5) M_{\odot}$ and the mass ratio $q \leq 0.08$. Inserting these two values in Equation (1.9) allows estimation of the mass of the central object. The mass function of the MQ itself is the bottom limit of the BH mass. The only unknown is the system inclination. However, there are boundaries within which the inclination should be found. The upper limit is 60° due to the absence of occultation by the companion star. The lower limit is set to $\sim 20^{\circ}$, because below this limit the resulting mass would be unreasonably high.

When looking for the most recent articles and results in constraining the parameters of GX 339-4, the values tend to vary. Most papers accept a high BH spin, $0.95_{-0.08}^{+0.02}$ (Parker et al., 2016), >0.97 (Ludlam et al., 2015) or $0.95_{-0.05}^{+0.03}$ (García et al., 2015). However, the results for the inclination are not that consistent: $30^{\circ} \pm 1^{\circ}$ (Parker et al., 2016), $36^{\circ} \pm 4^{\circ}$ (Ludlam et al., 2015), $48^{\circ} \pm 1^{\circ}$ (García et al., 2015). The mass estimates can be found within these values: $(6.8 \pm 1.64) M_{\odot}$ (Sreehari et al., 2015), $9.0_{-1.2}^{+1.6} M_{\odot}$ (Parker et al., 2016), $(7.5 \pm 0.8) M_{\odot}$ (Chen, 2011). Higher masses are acquired if the previously mentioned inclinations are used in combination with the mass function.

The aim of this work is to re-approach the estimates of parameters of GX 339-4. The inclination will be acquired by the RELXILL model, then combined with the mass function and compared with the mass parameter of the BHSPEC model. To verify the procedure, the same steps will be performed for the Cyg X-1 MQ.

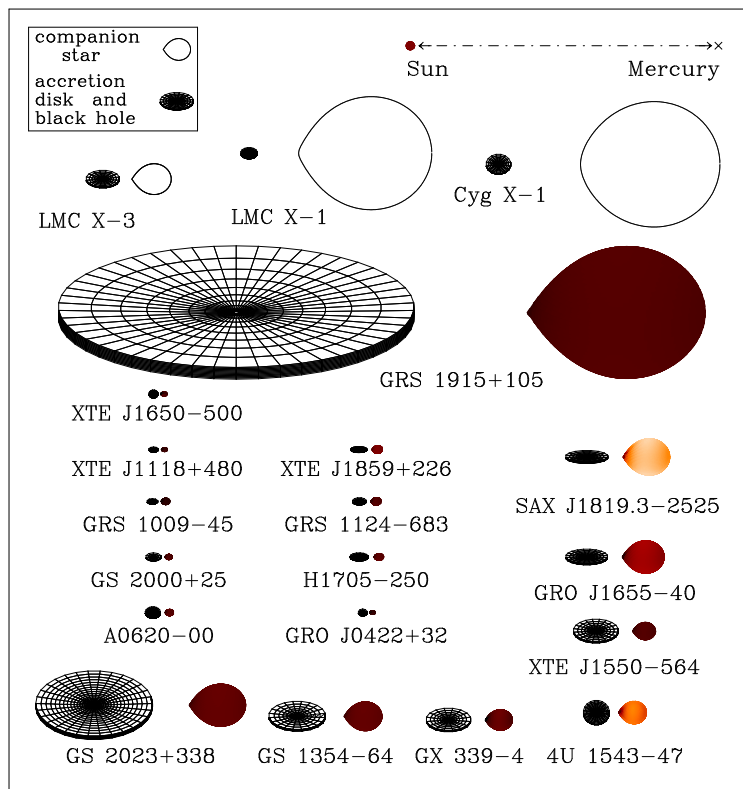


Figure 2.1: Illustrated comparison of selected MQs [e2]

2.2 Cyg X-1

This name belongs to one of the first discovered BHs. It was first detected by Geiger counters placed on two suborbital rockets in 1964 and then confirmed by observations made by the Uhuru satellite in 1971. Cyg X-1 is a part of a High Mass X-ray Binary system (HMXB). The spectral class of the donor star is O9.7I (blue massive supergiant). It is located in the Cygnus constellation at coordinates $\alpha = 19^{\circ}58'21.67''$ and $\delta = 35^{\circ}12'05.7''$.

The mass of the donor star is believed to be $\geq 20 M_{\odot}$. The most recent estimates are $19.2 M_{\odot}$ (Orosz et al., 2011) and $27 M_{\odot}$ (Ziółkowski, 2014). As for the mass of the BH, the former article mentions $14.8 M_{\odot}$ and the latter mentions $16 M_{\odot}$. These two articles also agree that the inclination cannot differ much from 30 degrees. Most articles also mention high BH spin, e.g. 0.988 (Tomsick et al., 2014).

As this MQ is a HMXB, the mass flow is not very concentrated and it may get into the LOS and cause variable absorption, which may complicate fitting procedures. (Grinberg et al., 2015) The most important parameter for this work is the mass function of Cyg X-1. Its value is 0.251 ± 0.007 with the mass ratio being 2.78 ± 0.39 (Gies et al., 2003).

Detectors

This work uses datasets from two X-ray missions, each requiring a different approach. This chapter provides a brief description of the missions and their detectors, followed by an explanation of the steps needed to obtain ready-to-use data. These sections are supposed to serve as a cookbook and contain basic data retrieval and reprocessing procedures. Where explanations would take up much space, a link to a relevant source is provided instead.

3.1 Suzaku

The Suzaku satellite (previously intended name Astro-E2) was a result of cooperation between NASA and JAXA agencies. The mission lasted from 2005 to 2015 and despite a major failure right after the launch, when the cooling medium boiled off to the open space, it produced a significant amount of data. The lost liquid helium was supposed to cool the primary instrument of the spacecraft, the X-Ray Spectrometer (XRS), which was therefore lost. Fortunately, four X-Ray Imaging Spectrometers (XIS) and the Hard X-ray Detector (HXD) remained operational and unaffected. The circular orbit had a radius of 550 km and inclination was 31 degrees. In September 2015 the radio transmitters were deactivated by JAXA and the mission officially ended.

The HXD was a collimated non-imaging instrument with an energy range from 10 keV up to 600 keV. It consisted of two detectors, PIN (< 50 keV) and GSO (> 50 keV). The four XIS instruments were imaging detectors and their energy range was from 0.2 keV to 12 keV with $18' \times 18'$ field of view. One XIS unit (XIS1) contained a back-side illuminated CCD chip, the other three contained front-side illuminated chips. Spectra of these three XIS units (XIS0, XIS2 and XIS3) can be combined together. However, the XIS2 instrument became unusable in November 2006, leaving only XIS0 and XIS3 to be combined.

The tasks needed to process the data from the Suzaku are all contained in the HEASOFT package. The software can be installed from a pre-compiled binary, or from the source code [e3]. All installation guides are provided at the download page.

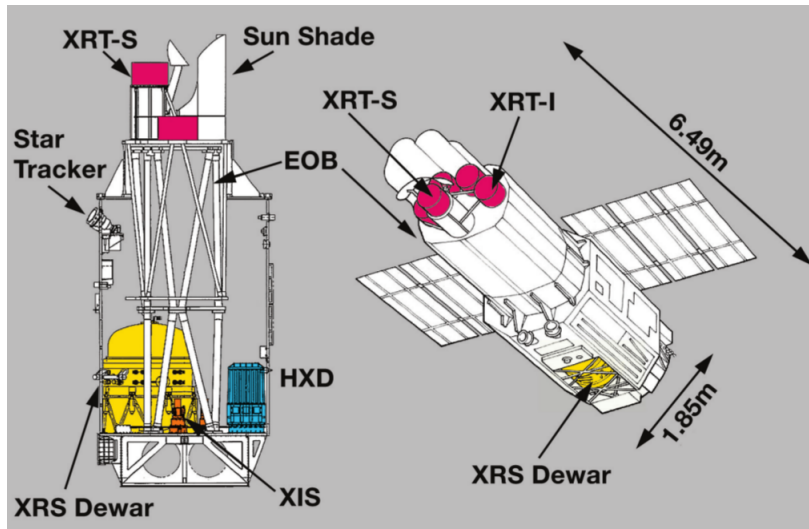


Figure 3.1: The Suzaku craft. EOB stands for Extendable Optical Bench and XRT are X-Ray Telescopes, one for the XRS and four for the XIS instruments. [e4]

3.1.1 Data retrieval

There are several ways to retrieve data, but only the procedures used in this work will be described. The data to be downloaded can be searched for with the HEASARC Browse interface. [e5] The first step is to specify the object by its name or position, the next step is to choose the mission. In this case the Suzaku. After launching the search, choose the Suzaku Master Catalogue, simply check the observations you are interested in and click the link at the bottom to retrieve data products. Next, you can choose the way you want to download the data, for example to create a download script using `wget`.

The Suzaku data follow file organisation described in the Suzaku ABC guide [e6]. The main interest lies in `event_cl` folders for each detector. These folders contain event files filtered with default settings. Unfiltered files for application of different settings are available in the `event_uf` folder.

3.1.2 Spectrum extraction

The spectrum extraction process differs for each of the Suzaku's instruments. This work uses only data from XIS and PIN instruments. The steps needed to obtain data from the GSO instrument are contained in the Suzaku ABC guide [e6]. The XIS is an imaging instrument, so user needs to choose regions for both the source and for the background to be extracted. For the PIN instrument, which is non-imaging, the background data are available from an ftp, where the data are stored by the year and the month of the observation.

`ftp://legacy.gsfc.nasa.gov/suzaku/data/background/pinnxb_ver2.0_tuned/`

XIS instrument

In the *xis/event_cl* folder, there are data from all the XIS instruments used for a particular observation. Moreover, data for each XIS instrument can be divided into multiple files with different editing modes (5x5, 3x3 and 2x2). Data for a XIS instrument with editing modes 5x5 and 3x3 should be combined in order to obtain the full exposure. However, data in the 2x2 editing mode should be dealt with separately. The spectra are extracted using the `xselect` command and then combined using the `addascaspec` command.

We provide an example of input for the `xselect` command. First, a session name is stated, followed by a command to read the event files (in the case of only one event file use `read event`). The dot selects the current folder and then a list of event files is inserted. The rest of the commands contains loading the region file, extracting the spectrum, saving it, repeating the same steps for the background spectrum. It is convenient to store these following commands in a text file which can be forwarded to the `xselect` command:

```
x3
read events
.
ae401068010xi3_0_3x3b099a_cl.evt.gz \
  ae401068010xi3_0_5x5b099a_cl.evt.gz
filter region x3_ds9.reg
extract spectrum
save spectrum resp=yes
spec_x3
yes
filter region -x3_ds9.reg
filter region x3_ds9_bg.reg
extract spectrum
save spectrum resp=no
spec_x3_bg
yes
```

After doing this for the XIS0 and XIS3 instruments, the spectra can be combined by creating a file that contains a list of the spectra, *fi.add*, which has this structure:

```
spec_x0.pha spec_x3.pha
spec_x0_bg.pha spec_x3_bg.pha
spec_x0.rsp spec_x3.rsp
```

This file is then used as an input for the `addascaspec` command in order to merge the spectra of two XIS instruments into one spectrum. In this example, the resulting spectrum is named *fi.pha*, the background spectrum *fi_b.pha* and the response matrix file *fi.rsp*.

```
addascaspec fi.add fi.pha fi.rsp fi_b.pha
```

PIN instrument

In order to extract a spectrum from PIN instrument data, a background event file has to be downloaded from the ftp mentioned at the beginning of this section. Once the file is present, the process is quite straightforward, in the case of using the pre-filtered data in *hxd/event_cl* folder. The command `hxdpinxbpi` requires four input parameters. These are a HXD cleaned PIN event file, a HXD cleaned PSE event file, a HXD PIN NXB event file and a name for the spectrum file.

3.2 XMM Newton

This mission was launched by ESA in 1999 and despite the original mission lifetime expectancy of only two years, the satellite is still operational. The mission has been extended to December 2018. The name stands for X-ray Multi-Mirror and soon after the launch the name Newton was added.

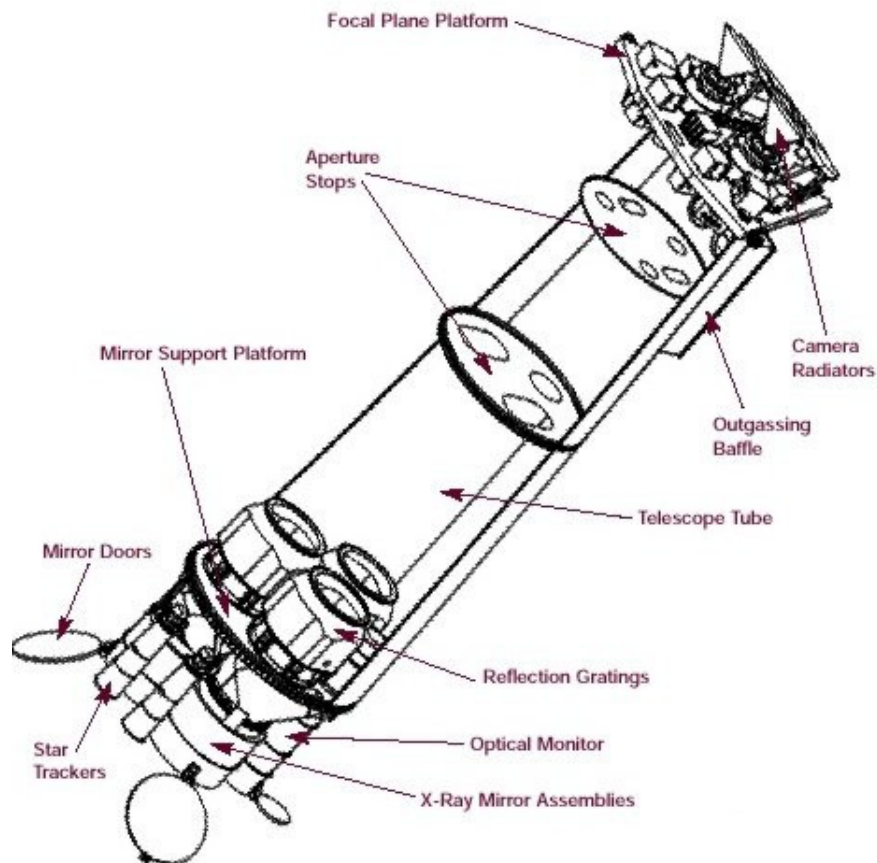


Figure 3.2: The XMM spacecraft [e7]

The orbit of the spacecraft is strongly eccentric, with $e \approx 0.788$. Figure 3.2 shows the spacecraft of the mission. On board, three instruments can be found. The Optical Monitor (OM) observes the same regions as the X-ray telescopes and provides complementary data in optical and UV band. The telescope of the OM is 2 meters long, 30 cm wide and provides a $17'$ field of view.

The other two instruments are the European Photon Imaging Camera (EPIC) and the Reflection Grating Spectrometer (RGS). One EPIC detector is placed behind each of the three X-ray telescopes seen in Figure 3.2. The EPIC instrument is an advanced CCD camera capable of registering weak X-ray radiation with very high time resolution. There are two kinds of EPIC detectors on board the XMM, one EPIC-PN detector and two EPIC-MOS detectors.

The EPIC-PN detector is made up of one CCD chip divided into 12 subunits. The energy range of this detector is from 0.2 keV to 15.0 keV. The EPIC-MOS detector is made up of 7 CCDs – middle one in the center of the focal plane, outer six stepped towards the mirror in order to cope with the curvature of the focal plane. The energy range of the EPIC-MOS detector is from 0.2 keV to 10.0 keV. The detectors are shown in Figure 3.3.

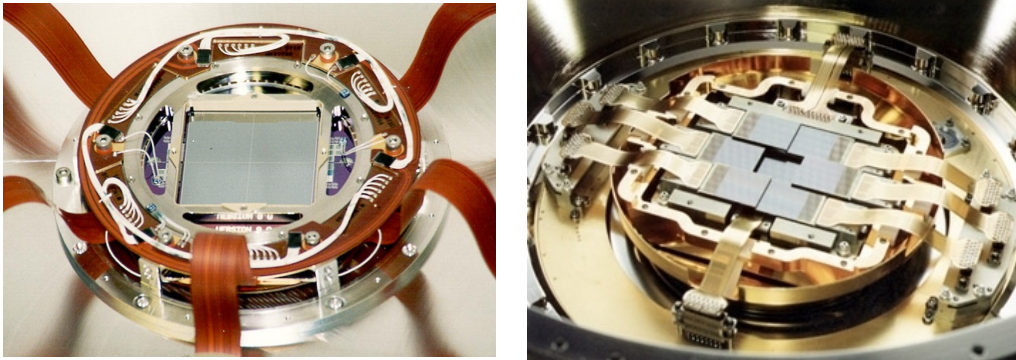


Figure 3.3: The EPIC detectors of XMM Newton. The EPIC-PN (left) and the EPIC-MOS (right) [e7]

The EPIC instrument can operate in different modes. The imaging mode can be reduced to a smaller region of the CCD chip in order to speed up the readout process. These modes are called Full frame, Large/Small Window. When very high time resolution is needed, the readout process merges one axis and creates a one dimensional image. This operation is called the timing mode. The EPIC-PN detector is also capable of operation in a special burst mode, which provides higher time resolution in exchange for a short duty cycle. The modes are presented in Figure 3.4.

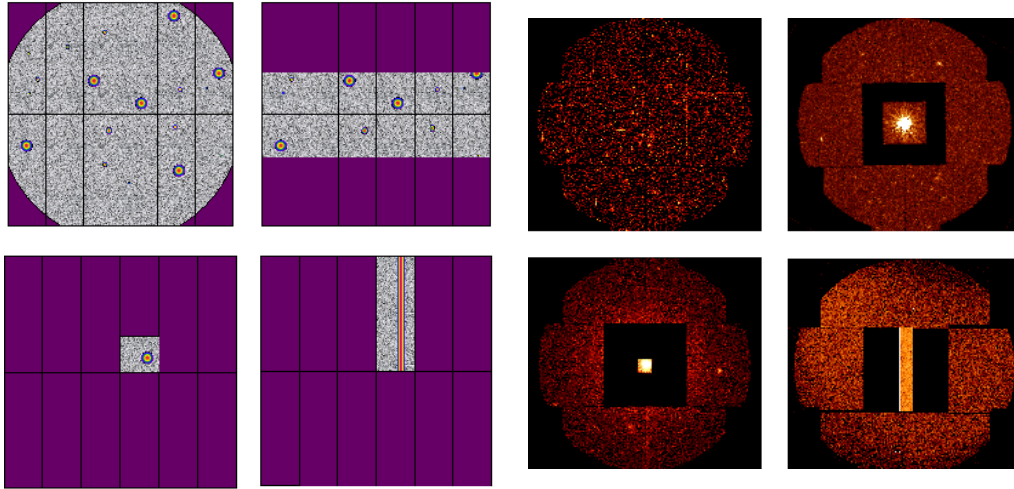


Figure 3.4: The modes of the EPIC instrument. Full frame, large window, small window and timing mode for EPIC-PN (left) and EPIC-MOS (right). [e7]

The RGS instrument is placed in front of both EPIC-MOS detectors and disperses approximately 44 % of the radiation. The rest reaches the EPIC-MOS detectors. The RGS instrument uses reflection gratings, which deflect the radiation to a strip of nine CCDs, where the position and energy of each detected photon is stored. The position serves to obtain the high resolution X-ray spectrum and the energy helps to resolve overlapping grating orders. The energy range of the RGS is from 0.33 keV to 2.5 keV with the resolution $E/\Delta E$ from 200 to 800.

3.2.1 Data retrieval

The XMM archive is accessible through ESA's XMM-Newton Science Archive [e8]. However, in order to be able to download multiple observations an account has to be created. Then the data can be searched for using a simple form. After choosing observations, a temporary link to an ftp archive is sent to the account's email address.

3.2.2 Spectrum extraction

In addition to the HEASOFT package, XMM data require another software package called XMM SAS. This software package can be downloaded from [e9], where an installation guide is provided as well. Once HEASOFT and XMM SAS have been initialised, the following steps are setting the `SAS_ODF` variable to the `odf` folder of an observation. Then, within the `odf` folder, `cifbuild` command has to be launched in order to create a calibration file `ccf.cif`. Another variable called `SAS_CCF` has to be set as the path to this calibration file. Then `odfingest` command is launched.

Following commands vary depending on whether MOS or PN data are to be extracted, alongside with the mode of the instruments. Only the steps needed in this work are mentioned. To summarise the previous comments:

```
cd 0112770101/odf
export SAS_ODF=$PWD
cifbuild
export SAS_CCF=$SAS_ODF/ccf.cif
odfingest
```

In order to extract a spectrum from the MOS instrument in imaging mode, create *mos* folder within the *odf* folder and in this folder run `emchain` and `mos-filter` commands. Amongst the output files, the filtered event files are named *mosXUYYYY-clean.fits* according to the number of the MOS instrument used. Afterwards, a region needs to be determined for both source and background areas of the image. Following commands needed to extract the source spectrum, background spectrum, response matrices and group them together are listed in Appendix A, as “MOS in imaging mode”.

The steps needed to extract a spectrum from the PN instrument in imaging mode are different. Instead of `emchain`, the command `epproc` is called. This creates an *ImagingEvs.ds* file, which then has to be filtered using these commands:

```
evselect table=2529_0692341201_EPN_S003_ImagingEvs.ds \
  withrateset=Y rateset=rateEPIC.fits maketimecolumn=Y \
  timebinsize=100 makeratecolumn=Y expression='#XMMEA_EP && \
  (PI>10000 && PI<12000) && (PATTERN==0)'
tabgtigen table=rateEPIC.fits expression='RATE<=0.4' \
  gtiset=EPICgti.fits
evselect table=2529_0692341201_EPN_S003_ImagingEvs.ds \
  withfilteredset=Y filteredset=EPICclean.fits destruct=Y \
  keepfilteroutput=T expression='#XMMEA_EP && \
  gti(EPICgti.fits,TIME) && (PI>150)'
```

These steps create a filtered event file named *EPICclean.fits*, which can be used for spectrum extraction. The commands are listed in Appendix A, as “PN in imaging mode”.

Spectrum extraction from the PN instrument in timing and burst mode require setting the source and background region in physical coordinates of the chip. The event files are the same as for the PN in imaging mode, except the event files are named *TimingEvs.ds*. After the event files are filtered, spectra can be extracted. The steps for timing mode and burst mode are listed in Appendix A, as “PN in timing mode” and as “PN in burst mode” respectively.

Data retrieval and reduction

4.1 GX 339-4

4.1.1 XMM Newton

The observations of GX 339-4 by XMM Newton are summarised in Table 4.1. The observations with PN in burst or timing mode were processed as described in the previous chapter. The regions used for spectrum extraction for MOS or PN in imaging mode are shown in Figure 4.1 and Figure 4.2 respectively.

Since the MOS instrument can work in different imaging modes, the used regions differ as well. Figure 4.1 present full window mode, with a circular region with a radius of $36''$ centred at the object and a circular region of the same radius in the right bottom corner of the same chip to extract the background spectrum. In the case of small window, the region to extract the background data was placed in the middle right chip with a radius of $45''$.

For the PN instrument in imaging mode, Figure 4.2 shows the extraction regions. For the source, the region has a radius of $19''$ and for the background data the region has a radius of $33''$.

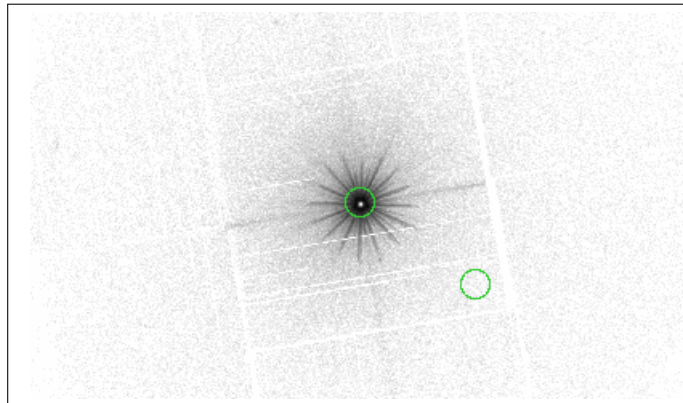


Figure 4.1: Regions used to extract data from GX 339-4 captured by XMM Newton's MOS instrument.

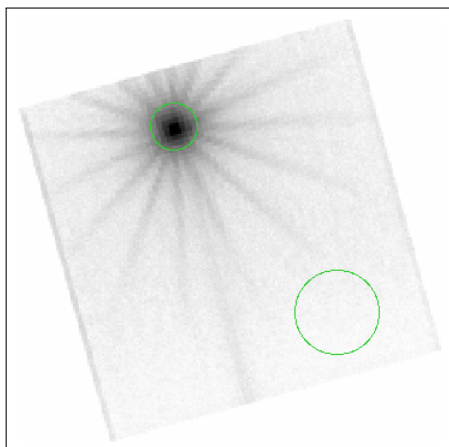


Figure 4.2: Regions used to extract data from GX 339-4 captured by XMM Newton's PN instrument.

Obs ID	Y/M	MJD	Duration (s)	PN	cts/s (PN)	cts/s (MOS)
0093562701	2002/08	52510.43769	61353	–	–	407.8
0148220201	2003/03	52706.74317	20500	ti	806	–
0148220301	2003/03	52718.06709	16271	ti	960	–
0156760101	2002/09	52546.37275	76339	–	–	236.1
0204730201	2004/03	53080.65307	137908	–	–	16.33
0204730301	2004/03	53082.63814	138480	–	–	19.58
0410581201	2007/02	54150.01451	15754	bu	5170	–
0410581301	2007/03	54164.48149	16702	bu	4073	–
0410581701	2007/03	54189.62578	18294	bu	2267	–
0605610201	2009/03	54916.31370	33529	ti	116.7	–
0654130401	2010/03	55283.04339	34938	ti	993.5	–
0692341201	2013/09	56564.95078	13700	im	121.5	34.34
0692341301	2013/09	56565.93719	15000	im	130.9	27.55
0692341401	2013/10	56566.76770	23000	im	112.3	32.09

Table 4.1: Observations of GX 339-4 made by XMM Newton

4.1.2 Suzaku

Observations of GX 339-4 by Suzaku are summarised in Table 4.2. Data filtered with default settings from *event_cl* were used. For each observation, a circular region with a radius of 260" centred at the object was used to extract the spectrum and a smaller circular region with a radius of 100" located in the top of the image was used to extract the background spectrum. Figure 4.3 shows the regions for the observation 401068010 (XIS0). The instrument XIS1 was not used and where both XIS0 and XIS3 were present, they were combined to obtain the resulting spectrum.

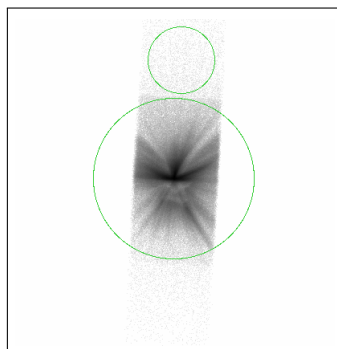


Figure 4.3: Regions used to extract data from GX 339-4 captured by Suzaku.

Obs ID	Y/M	MJD	Duration (s)	cts/s (XIS)	cts/s (PIN)
401068010	2007/02	54143.23161	77205.3	483.9	13.15
403011010	2009/03	54908.07862	43040.8	23.7	3.691
403011020	2009/03	54915.34306	39079.2	24.78	3.763
403011030	2009/03	54920.47740	39638.4	22.76	3.473
403067010	2008/09	54733.94265	104994.0	2.5	0.2231
405063010	2011/02	55603.76347	22459.4	28.39	1.339
405063020	2011/02	55608.96861	21015.7	13.19	0.9711
405063030	2011/02	55616.82337	19182.0	4.966	0.4115
405063040	2011/02	55620.17787	21799.0	3.653	0.3173
405063050	2011/03	55627.54685	16992.5	2.609	0.2293
408034010	2013/08	56526.57270	101019.6	34.56	3.487

Table 4.2: Observations of GX 339-4 made by Suzaku

4.2 Cyg X-1

4.2.1 XMM Newton

All observations of the Cyg X-1 MQ made by the XMM Newton mission presented in Table 4.3 were captured by the PN instrument. However, no observation was made with the PN instrument in imaging mode. The instrument was operating in either burst or timing mode. All data was processed using the same procedures as those used for the GX 339-4 MQ.

Obs ID	Y/M	MJD	Duration (s)	PN	cts/s (PN)	cts/s (MOS)
0202400101	2004/04	52510.43769	11369	ti	1694	–
0202400601	2004/04	52706.74317	11371	ti	1475	–
0202401101	2004/10	52718.06709	18221	bu	9651	–
0202401201	2004/10	52546.37275	18239	bu	7215	–
0500880201	2008/04	54189.62578	59438	ti	719.3	–
0610000401	2009/05	55283.04339	24941	bu	1414	–

Table 4.3: Observations of Cyg X-1 made by XMM Newton

4.2.2 Suzaku

Table 4.4 contains all observations of the Cyg X-1 by the Suzaku mission used in this work. The radii for the source and for the background regions were the same as for the GX 339-4 MQ and an example of the regions is shown in Figure 4.4.

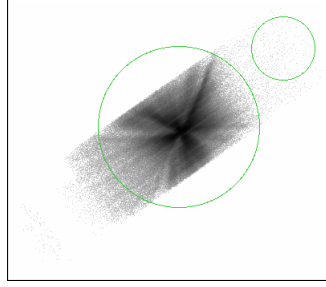


Figure 4.4: Regions used to extract data from Cyg X-1 captured by Suzaku.

Obs ID	Y/M	MJD	Duration (s)	cts/s (XIS)	cts/s (PIN)
401059010	2006/10	54038.15012	27706.8	224.4	39.37
402072010	2007/04	54220.81636	45320.4	163.5	27.7
402072020	2007/05	54237.82040	33356.8	105.7	17.54
403065010	2008/04	54574.68168	33943.5	198.4	33.27
404075010	2009/04	54924.05373	15309.1	263.2	35.43
404075020	2009/04	54929.25628	21336.1	260.2	34.05
404075030	2009/04	54935.76504	17108.8	210.9	30.16
404075050	2009/04	54949.70998	20521.2	212.5	30.34
404075060	2009/05	54957.70068	19434.5	314	35.21
404075070	2009/12	55182.06193	22101.9	301.8	46.35
404075080	2009/05	54971.02425	21340.4	278	31.23
404075090	2009/05	54976.35820	20925.2	379.1	38.44
404075100	2009/05	54980.49567	28784.5	347.6	34.91
404075110	2009/06	54984.48140	17450.2	590.3	43.56
404075120	2009/06	54986.82083	16873.3	423.1	35.36
404075130	2009/10	55125.37721	20498.5	242.4	26.1
404075140	2009/10	55130.26523	23104.2	233.9	27.37
404075150	2009/11	55138.89461	22616.8	138.9	21.43
404075160	2009/11	55145.81939	26022.2	142.9	21.07
404075170	2009/11	55152.28550	23448.5	260.7	36.81
404075180	2009/11	55159.51422	21768.5	294	30.8
404075190	2009/12	55166.29224	22415.5	273.9	30.76
404075200	2009/12	55173.64734	20016.6	189.6	30.07
406013010	2011/10	55839.92450	3702.7	1279	10.85
407015010	2013/04	56390.09534	4149.9	1345	8.552
407015020	2013/05	56419.09255	1512.4	1206	5.127
407072010	2012/10	56231.34167	372.6	2176	7.743
905006010	2010/12	55546.95622	461.2	1007	4.074

Table 4.4: Observations of Cyg X-1 made by Suzaku

GX 339-4

All spectra of GX 339-4 were first fitted with the simple `TBabs*(diskbb+power)` model to determine the temperature of the disk T_{in} and the power law index Γ . Results are listed together with the HR in Table 5.1 for the XMM data and in Table 5.2 for the Suzaku data. The HR was calculated for the count rate from 5.0 keV to 10.0 keV divided by the count rate from 0.5 keV to 2.0 keV (values taken from Parker et al. (2015)) and then normalised (factor 0.4 for XMM and 0.55 for Suzaku).

Obs ID	EPIC	HR	T_{in}	Γ	Reduced χ^2
0093562701	MOS	0.193	0.9368	2.29	1.69
0148220201	PN	0.08	0.4826	2.76	8.89
0148220301	PN	0.05	0.5355	2.89	12.89
0156760101	MOS	0.207	0.8839	2.13	5.99
0204730201	MOS	0.733	0.2544	1.35	4.64
0204730301	MOS	0.72	0.2519	1.39	4.85
0410581201	PN	0.12	0.8759	3.01	1.83
0410581301	PN	0.163	0.7964	2.57	2.08
0410581701	PN	0.05	0.6785	3.23	1.77
0605610201	PN	0.977	0.2395	1.50	4.92
0654130401	PN	0.837	0.2654	1.62	91.93
0692341201	PN	0.9	0.1697	1.46	1.22
0692341201	MOS	0.723	0.2632	1.34	2.22
0692341301	PN	0.88	0.1864	1.46	2.16
0692341301	MOS	0.73	0.2523	1.35	2.42
0692341401	PN	0.92	0.1815	1.46	2.34
0692341401	MOS	0.727	0.2595	1.35	3.51

Table 5.1: XMM Newton observations of GX 339-4 with simple model parameters

Unfortunately, new X-ray missions focus mainly on quality of data rather than on quantity. Results from Table 5.1 cannot be presented in the form of a HID, mainly because it contains data from two different instruments or different observation modes. However, Table 5.2 can be used to create a sparse HID, shown in Figure 5.1. Most Suzaku observations of GX 339-4 were performed when the MQ was in the hard state. Despite the fact that no soft state data are present, two observations capture GX 339-4 in distinctive intermediate states.

Obs ID	HR	T_{in}	Γ	Reduced χ^2
401068010	0.27	0.755	2.01	11.44
403011010	0.88	0.401	1.39	2.22
403011020	0.87	0.412	1.39	2.24
403011030	0.87	0.431	1.37	2.22
403067010	0.93	0.598	1.51	1.25
405063010	0.43	0.315	1.75	1.84
405063020	0.69	0.283	1.60	1.43
405063030	0.88	0.483	1.53	1.12
405063040	0.91	0.601	1.53	1.06
405063050	0.91	0.629	1.55	0.99
408034010	0.88	0.326	1.45	6.98

Table 5.2: Suzaku observations of GX 339-4 with simple model parameters

In comparison with the HID in Figure 1.2, the observation 401068010 from Table 5.2 is located near the observations of GX 339-4 in SPL state. However, the parameters do not meet the conditions of the SPL state, but it still appears to contain the reflection component. Figure 5.2 shows that a simple power law model cannot describe this spectrum. The offset around the 20 keV is caused by the Compton hump typical for the reflected radiation.

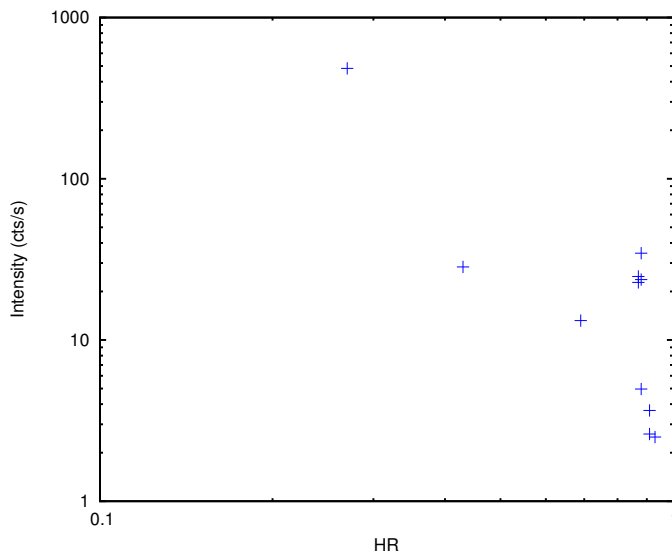


Figure 5.1: HID of Suzaku observations of GX 339-4

In Figure 5.2, there are many line-like features around 2 keV. These features have origin in the instrument. There are both absorption features, e.g. K-shell line of aluminium (1.56 keV), and emission features, mainly M-shell lines from gold in the XRT instrument around 2 keV. ([ex]) These features can be fitted with simple Gaussian lines, but it is a common practice to leave them out from the fitting process.

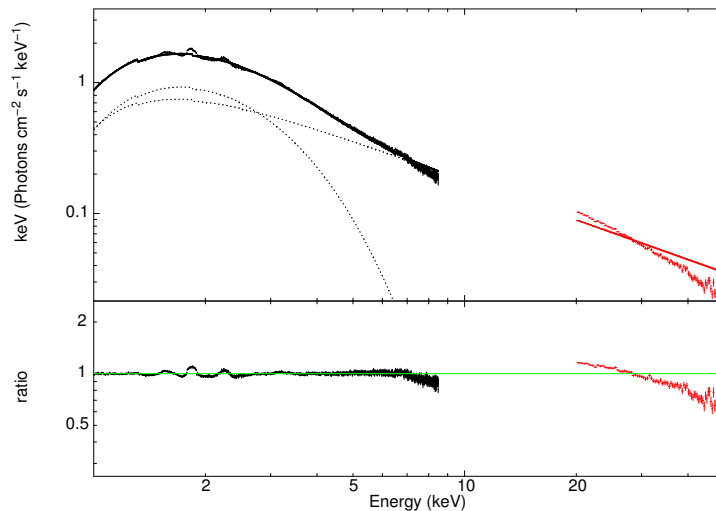


Figure 5.2: Spectrum of GX 339-4 folded with a simple model (407072010) and model to data ratio

5.1 Fitting reflection

The reflection component in Figure 5.2 allowed for use of the RELXILL model. This model was used together with an absorption model and a multi blackbody model for the observation 401068010. The results of fitting `TBabs*(diskbb+relxill)` are shown in Table 5.3. The column “input” contains parameter values or boundaries set before the fitting. Where empty, default values were used. Parameters R_{in} , R_{out} and z were frozen at their default value and *angleon* was set to 1. As for the instrument related features, regions 1.5–1.95 keV, 2.1–2.4 keV and 3.0–3.3 keV were omitted from the fitting process.

Model	Parameter	Input	Result	Error
TBabs	nH	0.5-0.65	0.587	0.006
DISKBB	Tin	0.1-1.5	0.828	0.006
DISKBB	norm	–	805.529	23.282
RELXILL	Index1	–	9.999	2.210
RELXILL	Index2	–	5.307	0.178
RELXILL	Rbr	–	1.861	0.066
RELXILL	a	–	0.997	0.004
RELXILL	Incl	20.0–60.0	50.199	1.189
RELXILL	gamma	–	2.137	0.011
RELXILL	logxi	–	2.783	0.025
RELXILL	Afe	–	0.981	0.057
RELXILL	refl_frac	–	10.007	3.010
RELXILL	norm	–	0.012	0.003

$\chi_{\text{red}}^2 = 1.376$ for 1055 DOF

Table 5.3: Model parameters for 401068010

The result is presented in Figure 5.3. The omitted parts of the spectrum (e.g. above 8.5 keV for the XIS data) were left out due to high uncertainties. The inclination of the disc is the most important result of this fit. It allows for the estimation of the BH mass from its mass function. Even though XSPEC by default works with the confidence level of 90%, an error of 2 degrees will be used for the inclination in order to include any other possible statistical errors. Using $f(M) = 5.8 \pm 0.5$ and $q = 0.08$, the resulting BH mass is $\approx 15 \pm 2.5 M_{\odot}$.

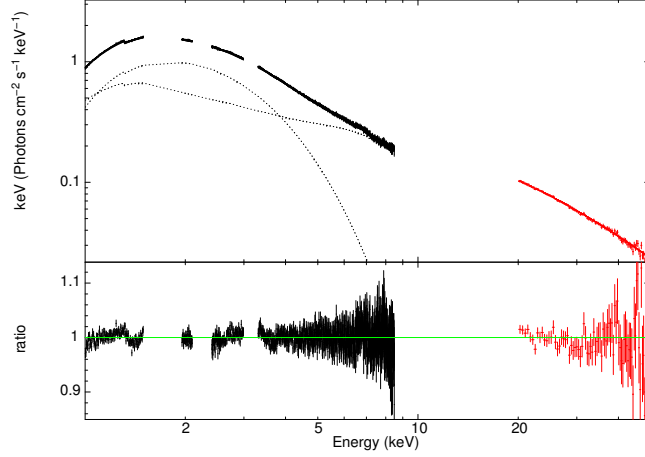


Figure 5.3: RELXILL model applied to 401068010 and model to data ratio

Figure 5.4 contains a contour from the `steppar` command of XSPEC for the inclination. It shows the local minimum for the fitting around the resulting inclination. This value was further used as an input parameter for the BHSPEC model in order to obtain a second BH mass estimate directly from this model.

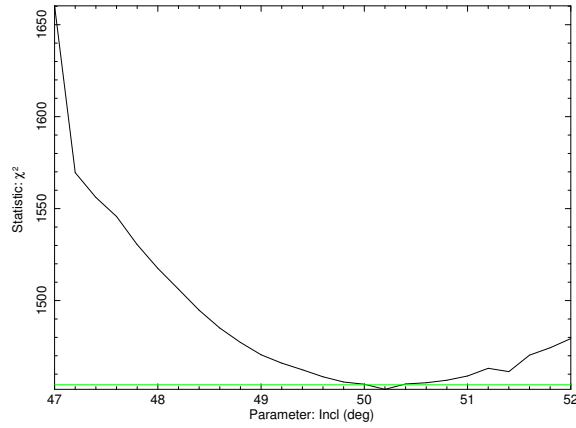


Figure 5.4: Contour of the `steppar` command for applied to Figure 5.3

5.2 BHSPEC fitting

The model combination `TBabs*(bhspec+power)` was first used for the same observation, but only for the XIS instrument data. The inclination, nH parameter and power law photon index were frozen at the values obtained from the RELXILL model. The other parameters were left free to vary.

This procedure was then repeated for multiple observations of the XMM Newton with only the inclination being frozen. In order to choose the observations suitable for this procedure, the conditions were set for the HR to be below 0.2 and the T_{in} to be above 0.6 keV. These conditions were met within these observations: 0093562701, 0410581201, 0410581301, 0410581701.

Table 5.4 contains parameters obtained from fitting the Suzaku observation 401068010 with the BHSPEC model. Again, there are parts of the spectrum around 2 keV energy that were left out. The spectrum is presented in Figure 5.5 (a) together with the `steppar` test (b) of the inclination. The `log mass` parameter is 1.048 ± 0.171 what gives BH mass $\approx 11.2 \pm 4.4 M_{\odot}$.

Model	Parameter	Input	Result	Error
TBabs	nH	0.587	0.587	–
BHSPEC	<code>log mass</code>	–	1.048	0.171
BHSPEC	<code>log lumin</code>	–	-1.075	0.062
BHSPEC	<code>inc</code>	0.640	0.640	–
BHSPEC	<code>spin</code>	–	0.792	0.057
BHSPEC	<code>norm</code>	–	0.596	0.294
POWERLAW	<code>PhoIndex</code>	2.137	2.137	–
POWERLAW	<code>norm</code>	–	2.254	0.005

$\chi_{\text{red}}^2 = 2.172$ for 1024 DOF

Table 5.4: Model parameters for 401068010

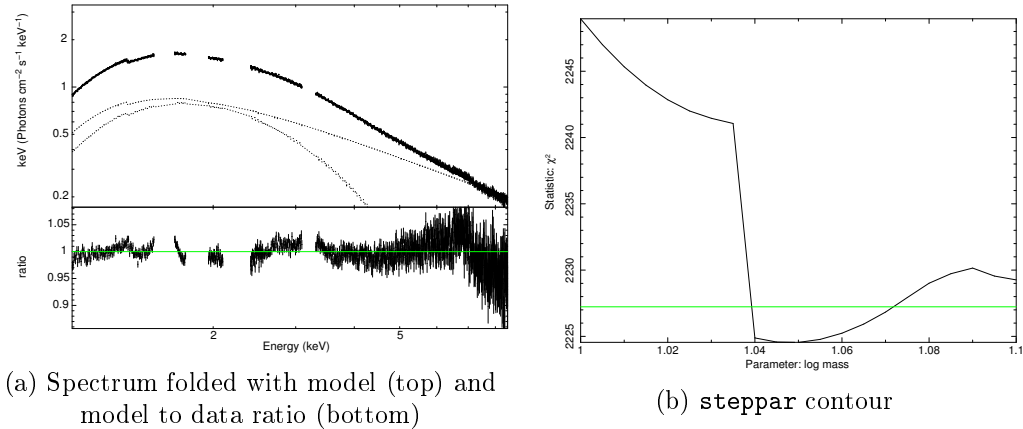


Figure 5.5: BHSPEC model applied to 401068010

Observation carried out by the XMM Newton used in this procedure required very individual approach. The data are from both PN and MOS instruments and both imaging and burst modes. The observations 0410581201 and 0410581701 were fitted using the same models combination as in the previous step. The results are listed in Table 5.5. The BH mass estimates are $14.1 \pm 5.4 M_{\odot}$ and $15.7 \pm 8.2 M_{\odot}$ for 0410581201 and 0410581701, respectively.

Observation ID		0410581201			0410581701		
Model	Parameter	Input	Result	Error	Input	Result	Error
TBabs	nH	0.5-0.7	0.629	0.012	0.5-0.7	0.680	0.026
BHSPEC	log mass	-	1.15	0.165	-	1.197	0.227
BHSPEC	log lumin	-	-1.249	0.106	-	-1.605	0.224
BHSPEC	inc	0.640	0.640	-	0.640	0.640	-
BHSPEC	spin	-	0.99	0.03	-	0.98	0.02
BHSPEC	norm	-	3.406	1.969	-	2.921	2.189
POWERLAW	PhoIndex	-	3.031	0.059	-	3.424	0.059
POWERLAW	norm	-	3.389	0.442	-	2.976	0.273
		$\chi^2_{\text{red}} = 1.313$ for 157 DOF			$\chi^2_{\text{red}} = 1.213$ for 144 DOF		

Table 5.5: Model parameters for 0410581201 and 041581701

The spectra are shown in Figure 5.6 for observation number 041058120 and in Figure 5.7 for observation number 0410581701. These two observations were carried out by the PN instrument in burst mode and were possible to be fitted with the TBabs*(bhspec+power) model.

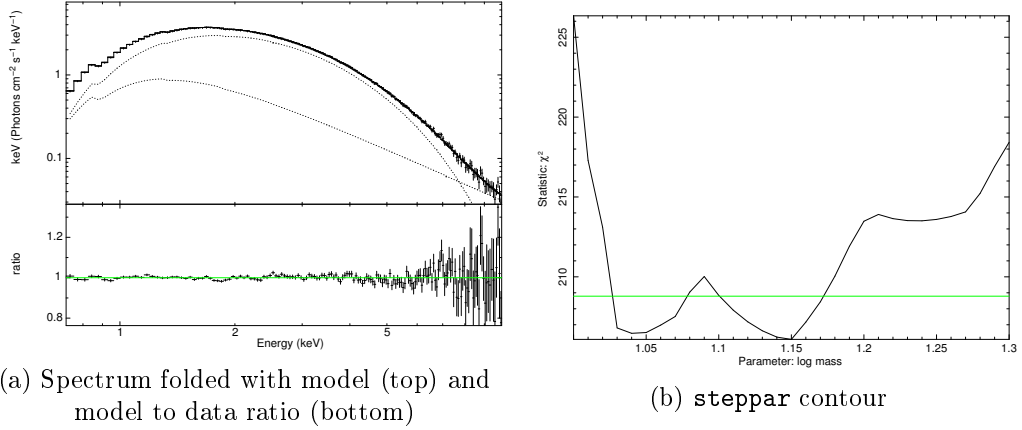


Figure 5.6: BHSPEC model applied to 0410581201

Again, the spectra with ratio data \times model and the contour of `steppar` command are present. In Figure 5.6 (b), the model seems to have two local minima close to each other. However, the error of the `log mass` parameter from Table 5.5 covers both values.

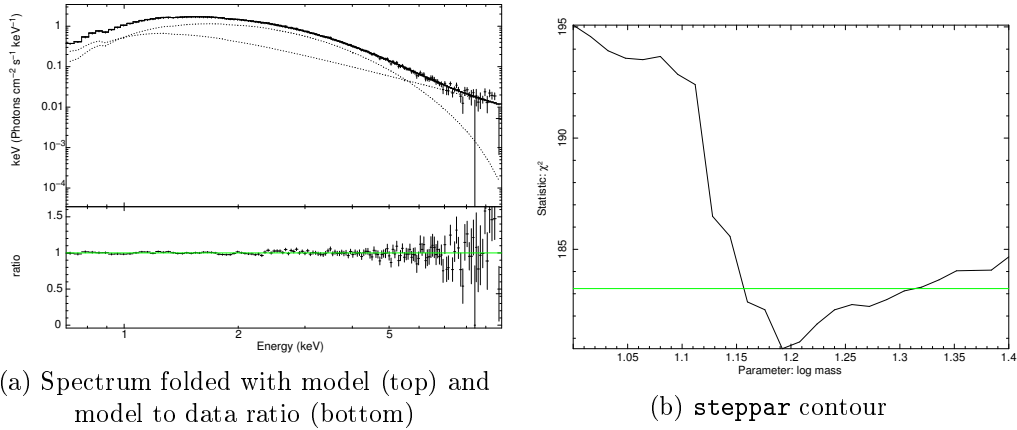


Figure 5.7: BHSPEC model applied to 0410581701

The shape of the spectrum in Figure 5.7 (a) appears to differ from the one in Figure 5.6 (a). The count rate of the observation number 0410581701 is lower as well as the value of HR. This might imply that the spectrum of observation number 0410581201 corresponds to the SPL state and the observation number 0410581701 was performed when the GX 339-4 was in the thermal state.

The two following observations required more complicated approach. The observation number 0410581301 is presented in Figure 5.8. Instead of a simple power law model, broken power law model had to be used in order to properly describe the spectrum. The break energy of the model is very near the iron $K\alpha$ line. Nonetheless, including the iron line models did not fit very well, so the broken power law model was used instead. The results are presented in Table 5.6. Using the `log mass` parameter value, the BH mass estimate for this observation number is $14.7 \pm 8 M_{\odot}$.

Model	Parameter	Input	Result	Error
TBabs	nH	0.5-0.7	0.642	0.007
BHSPEC	log mass	-	1.168	0.237
BHSPEC	log lumin	-	-1.389	0.246
BHSPEC	inc	0.640	0.640	-
BHSPEC	spin	-	0.983	0.021
BHSPEC	norm	-	2.186	1.709
BKNPOWER	PhoIndx1	-	2.608	0.035
BKNPOWER	BreakE	-	6.876	0.352
BKNPOWER	PhoIndx2	-	3.175	0.162
BKNPOWER	norm	-	5.174	0.358
$\chi^2_{\text{red}} = 1.359$ for 159 DOF				

Table 5.6: Model parameters for 041581301

It is noticeable that the count rate of this observation is higher than that seen in Figure 5.7. The observation number 0410581301 was performed when GX 339-4 was in a distinctive SPL state. This might be the reason of the high uncertainty of

the mass estimation. The BHSPEC model is most suitable for the thermal state, when the accretion disc extends down to the ISCO. In the case of a truncation of some innermost regions, the model might not be able to describe the spectrum very well. However, the contour presented in Figure 5.7 (b) shows a nice local minimum for the acquired `log mass` value, yet with large uncertainty.

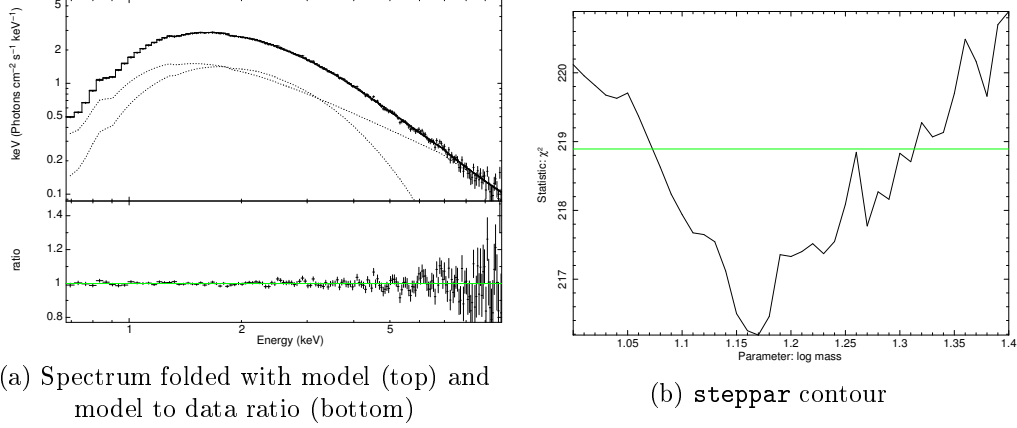


Figure 5.8: BHSPEC model applied to 0410581301

The last observation used in this procedure was 0093562701, where the spectrum was extracted from the MOS instrument operating in imaging mode. As this instrument has a smaller energy range, there are large uncertainties appearing at energies lower than for the PN instrument. Moreover, this spectrum required, besides the broken power law model, an addition of a Gaussian line due to an emission line-like feature near 8 keV.

Model	Parameter	Input	Result	Error
TBabs	nH	0.5-0.7	0.562	0.021
BHSPEC	log mass	–	1.293	0.214
BHSPEC	log lumin	–	-0.979	0.289
BHSPEC	inc	0.640	0.640	–
BHSPEC	spin	–	0.990	0.028
BHSPEC	norm	–	0.260	0.213
BKNPOWER	PhoIndx1	–	2.115	0.112
BKNPOWER	BreakE	–	102.99	4.352
BKNPOWER	PhoIndx2	–	1.987	0.254
BKNPOWER	norm	–	0.432	0.032
GAUSSIAN	LineE	7.5-8.5	7.960	0.108
GAUSSIAN	Sigma	–	0.571	0.159
GAUSSIAN	norm	–	0.005	0.002

$\chi_{\text{red}}^2 = 1.465$ for 129 DOF

Table 5.7: Model parameters for 0093562701

The results of the fit are presented in Table 5.7, where again the `log mass` parameter value has rather large uncertainty. This might be caused by the use of the Gaussian line due to the fact that the BHSPEC model appears to be very sensitive to a combination with other models. This result yields a BH mass estimate of $19.6 \pm 9.7 M_{\odot}$.

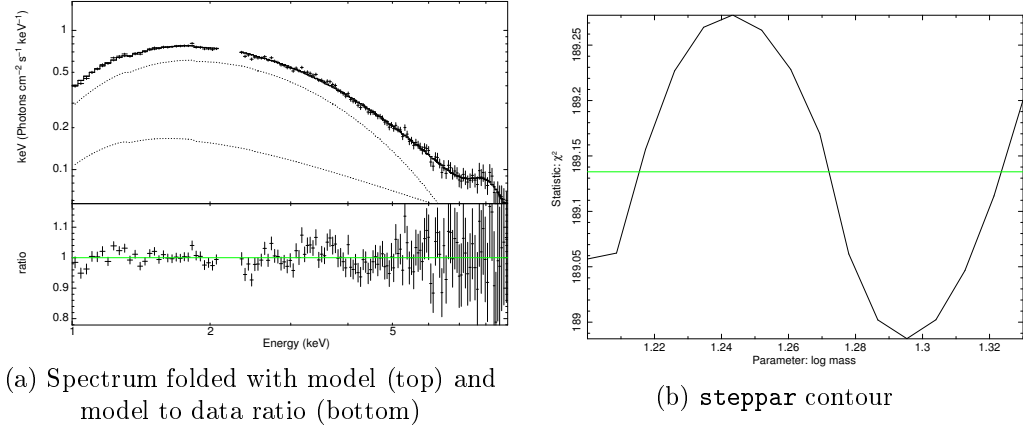


Figure 5.9: BHSPEC model applied to 0093562701

As seen in Figure 5.9 (a), a short range of data had to be excluded near 2.2 keV due to instrumental features. This exclusion served only to decrease the χ^2 test value and did not have a large effect on the output parameters. The contour in Figure 5.9 (b) shows that the minimum for the mass parameter was found, yet with rather high uncertainty and a better minimum at a lower value. Therefore, this particular result might be questionable.

Cyg X-1

The procedure from the previous chapter was repeated step by step. First, all spectra were fitted with a simple `TBabs*(diskbb+power)` model. The results are presented in Table 6.1 and in Table 6.2 for the Suzaku mission and the XMM Newton mission, respectively. The amount of data from the Suzaku mission allowed again a creation of a sparse HID presented in Figure 6.1. The HR in Table 6.1 was again normalised with a factor of 0.75 in order to extend to 1.

Obs ID	HR	T_{in}	Γ	Reduced χ^2
401059010	0.551	0.802	1.36	3.191
402072010	0.885	2.170	1.364	3.005
402072020	0.817	1.972	1.396	2.031
403065010	0.891	1.952	1.332	3.969
404075010	0.536	0.739	1.399	1.679
404075020	0.519	0.825	1.412	1.633
404075030	0.543	0.886	1.361	1.735
404075050	0.675	1.408	1.406	1.661
404075060	0.449	0.729	1.455	1.885
404075070	0.431	0.642	1.345	1.698
404075080	0.448	0.684	1.461	1.928
404075090	0.364	0.011	1.557	9.425
404075100	0.255	0.626	1.348	9.078
404075110	0.269	0.518	1.579	5.065
404075120	0.301	0.539	1.535	1.889
404075130	0.452	0.729	1.468	1.764
404075140	0.508	0.772	1.437	1.854
404075150	0.963	5.197	1.403	1.467
404075160	0.837	1.887	1.375	1.964
404075170	0.608	0.951	1.366	2.165
404075180	0.461	0.564	1.492	1.332
404075190	0.495	0.731	1.462	1.394
404075200	0.751	11.519	1.502	1.293
406013010	0.116	0.462	2.447	4.701
407015010	0.099	0.493	2.539	7.688
407015020	0.064	0.517	2.601	4.089
407072010	0.077	0.868	2.089	54.953
905006010	0.057	0.011	3.645	34.197

Table 6.1: Suzaku observations of Cyg X-1 with simple model parameters

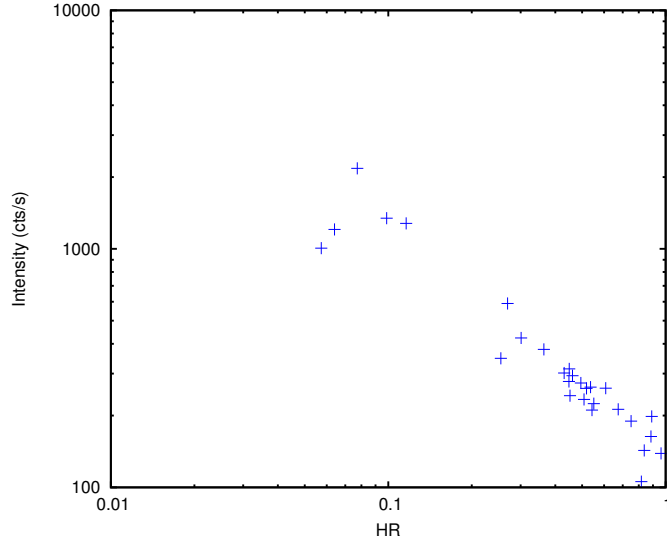


Figure 6.1: HID of Suzaku observations of Cyg X-1 (HR for the same energy bands as in Figure 5.1)

All the XMM Newton observations presented in Table 6.2 are from the PN instrument. The HR was normalised by a factor of 0.5 to fully extend the HR from 0 to 1. Two observations with the lowest HR could represent Cyg X-1 in the thermal state. This assumption was dealt with later, after searching for the inclination.

Obs ID	PN mode	HR	T_{in}	Γ	Reduced χ^2
0202400101	ti	0.169	0.302	1.99	11.18
0202400601	ti	0.190	0.242	1.96	3.53
0202401101	bu	0.089	0.005	3.23	33.24
0202401201	bu	0.065	0.408	2.48	8.56
0500880201	bu	0.903	2.588	1.39	3.62
0610000401	bu	0.378	0.004	1.79	13.53

Table 6.2: XMM Newton observations of Cyg X-1 with simple model parameters

In order to follow the procedure from the previous chapter, an observation carried out by the Suzaku had to be chosen based on the presence of the reflection component. Five bottom observations from Table 6.1 occupy left-top corner of the HID in Figure 6.1. However, applying the RELXILL model only worked well enough with the observation number 407072010. All the other observations did not contain the reflection component in a sufficient quality.

Figure 6.2 shows the spectrum of the particular observation folded with the simple `TBabs*(diskbb+power)` model. It is once again noticeable, that a simple power law function is incapable of describing the spectrum. However, the data for the Cyg X-1 MQ contain more features and distortions in the spectra. Therefore the energy ranges had to be adjusted separately for each observation.

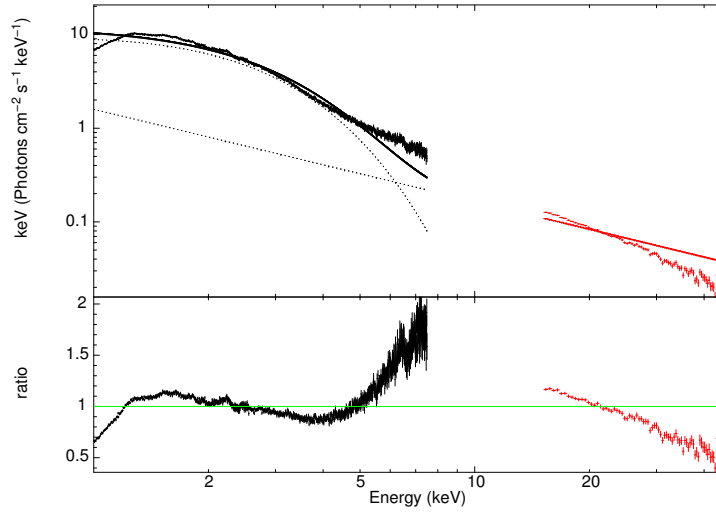


Figure 6.2: Spectrum of Cyg X-1 folded with a simple model (407072010) and model to data ratio

6.1 Fitting reflection

The selected observation of the Cyg X-1 MQ was used to obtain the inclination parameter from the RELXILL model. The process again required an exclusion of several energy bands due to the presence of the instrument related features in the spectrum. Nevertheless, there were many unidentified features in the spectrum, which made applying the model more difficult.

The parameters of the applied model are presented in Table 6.3, with the inclination being 52.2 degrees with a 1.3 degrees error. Again, this error was extended to 2 degrees to cover any unconsidered uncertainties.

Model	Parameter	Input	Result	Error
TBabs	nH	0.5-1.5	0.839	0.013
DISKBB	Tin	0.1-2.0	0.618	0.004
DISKBB	norm	–	12473.2	3339.1
RELXILL	Index1	–	4.612	0.232
RELXILL	Index2	–	9.992	4.335
RELXILL	Rbr	–	40.732	22.788
RELXILL	a	–	0.948	0.008
RELXILL	Incl	–	52.2	1.3
RELXILL	gamma	–	2.999	0.024
RELXILL	logxi	–	3.491	0.058
RELXILL	Afe	–	4.554	0.394
RELXILL	refl_frac	–	2.607	0.424
RELXILL	norm	–	0.784	0.209
$\chi^2_{\text{red}} = 1.714$ for 919 DOF				

Table 6.3: Model parameters for 407072010

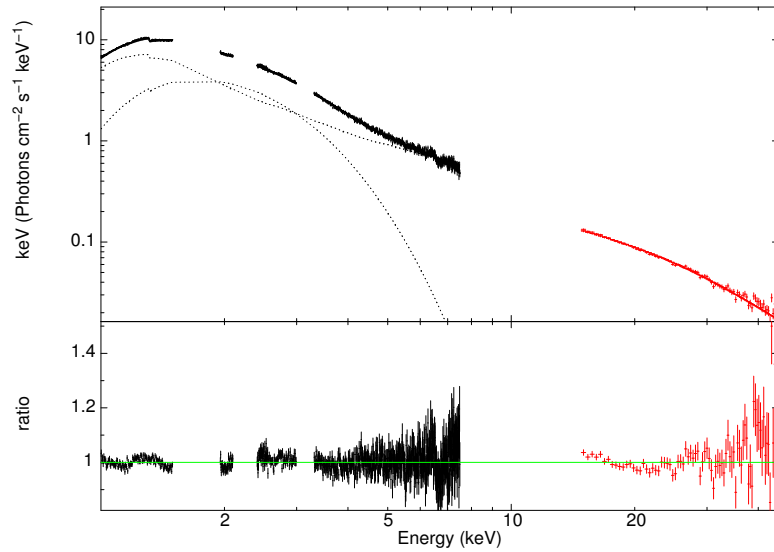


Figure 6.3: RELXILL model applied to 407072010 and model to data ratio

The mass function for Cyg X-1 is 0.251 ± 0.007 , with 2.78 ± 0.39 being the mass ratio. (Gies et al., 2003) Using the inclination derived from the RELXILL model, the resulting BH mass estimate is $7.3 \pm 2.6 M_{\odot}$. The inclination was used together with the BHSPEC model applied to other observation to obtain more BH mass estimates.

Despite the fact that Figure 6.4 shows a nice minimum for the inclination, the ratio in Figure 6.3 reveals that the model does not follow the spectrum that well. For example, it does not fit the iron line with sufficient precision and therefore, this result is very questionable and should be treated with caution.

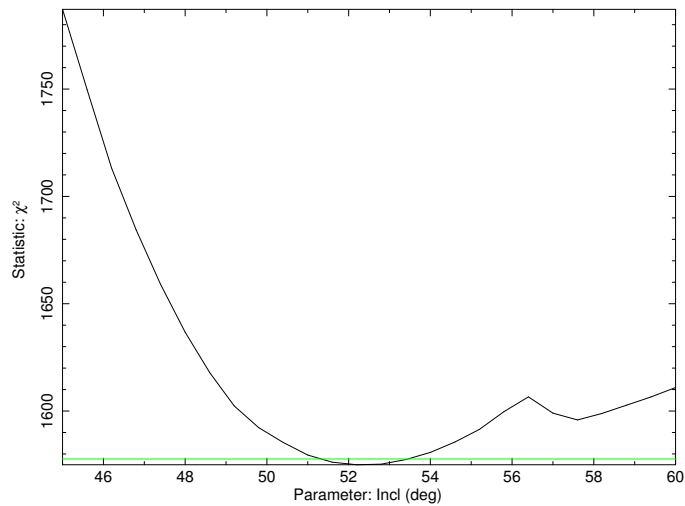


Figure 6.4: Contour of the `steppar` command for applied to Figure 6.3

6.2 BHSPEC fitting

The first step was to apply the BHSPEC model to the same observation that was used to determine the inclination. For GX 339-4, the hydrogen column density, photometric index and inclination parameters were fixed to the values of the RELXILL model. In this case, getting better results required for the hydrogen column density parameter to be released. The results of the fit are shown in Table 6.4.

Model	Parameter	Input	Result	Error
TBabs	nH	–	0.669	0.008
BHSPEC	log mass	–	0.877	0.247
BHSPEC	log lumin	–	-1.958	0.263
BHSPEC	inc	0.640	0.640	–
BHSPEC	spin	–	0.836	0.103
BHSPEC	norm	–	32.606	24.981
POWERLAW	PhoIndex	2.999	2.999	–
POWERLAW	norm	–	28.204	0.075

$\chi_{\text{red}}^2 = 2.651$ for 1124 DOF

Table 6.4: Model parameters for 407072010

The spectrum and the contour are shown in Figure 6.5. The iron line around 6.4 keV is very prominent. However, including it into the model with either LAOR model or just by a simple Gaussian line improved the χ^2 test, but worsened the errors of parameters, especially for the mass parameter. The contour in Figure 6.5 (b) shows that the acquired `log mass` value is in a very narrow minimum.

Despite the narrow minimum, the mass parameter has high error, which leads to the BH mass estimate of $7.5 \pm 4.3 M_{\odot}$. This uncertainty is very high in the sense that it could allow for the mass to drop down to the bottom limit of Cyg X-1 actually being a BH.

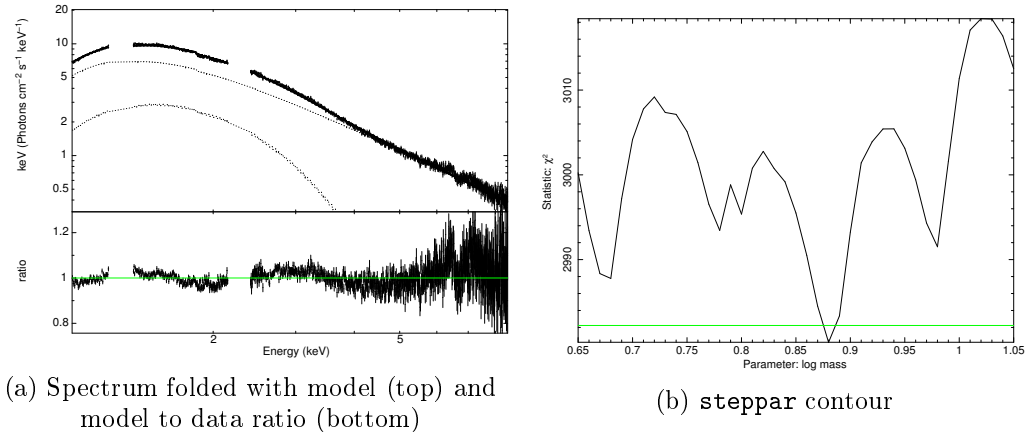


Figure 6.5: BHSPEC model applied to 407072010

The observation number 407015010 by the Suzaku satellite provided a very bad estimate for the BH mass. The parameters are presented in Table 6.5, where the error of the `log mass` parameter is extremely high. The fit itself is very inaccurate due to many unidentified features of the spectrum. Even the overall shape of the spectrum is in disagreement with the BHSPEC model. The process required an addition of a Gaussian line to stabilize the mass parameter. The final BH mass estimate is $7.5 M_{\odot}$. The error of the BH mass is unusable in this case.

Model	Parameter	Input	Result	Error
TBabs	nH	–	1.142	0.016
BHSPEC	log mass	–	0.893	0.645
BHSPEC	log lumin	–	-1.061	0.356
BHSPEC	inc	0.640	0.640	–
BHSPEC	spin	–	0.751	0.418
BHSPEC	norm	–	3.379	6.875
POWERLAW	PhoIndex	–	5.336	0.102
POWERLAW	norm	–	66.991	2.532
GAUSSIAN	LineE	–	6.268	0.041
GAUSSIAN	Sigma	1.779	0.039	–
GAUSSIAN	norm	–	0.281	0.011

$\chi_{\text{red}}^2 = 3.468$ for 1037 DOF

Table 6.5: Model parameters for 407015010

The most problematic feature in Figure 6.6 (b) is the unstable minimum for the `log mass` parameter. The acquired value is at a minimum that applies only to a small range of the parameter. The contour shows that there are values with better χ^2 test results. The ratio in Figure 6.6 (a) shows that the final folded model does not follow the data very well.

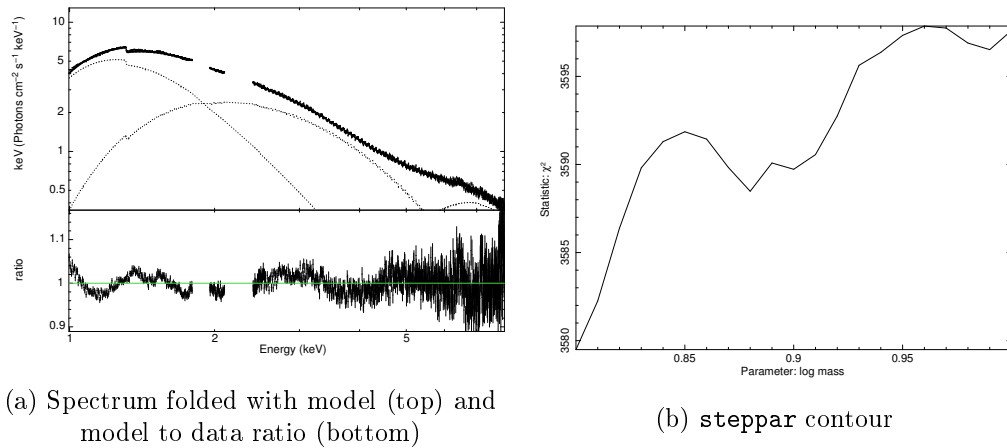


Figure 6.6: BHSPEC model applied to 407015010

Better results were obtained from applying the model to the observation number 407015020 made by the Suzaku satellite. Table 6.6 presents the values of the parameters. Instead of the simple power law, the broken power law was required to get the best fit. However, the `log mass` parameter still has a rather high error. The BH mass estimate is $23.5 \pm 17.1 M_{\odot}$.

Model	Parameter	Input	Result	Error
TBabs	nH	–	1.089	0.015
BHSPEC	log mass	–	1.371	0.317
BHSPEC	log lumin	–	-1.344	0.283
BHSPEC	inc	0.640	0.640	–
BHSPEC	spin	–	0.643	0.441
BHSPEC	norm	–	2.832	2.426
BKNPOWER	PhoIndx1	–	5.283	0.087
BKNPOWER	BreakE	–	1.984	0.012
BKNPOWER	PhoIndx2	2.787	0.022	–
BKNPOWER	norm	–	50.266	2.099

$\chi_{\text{red}} = 1.769$ for 1231 DOF

Table 6.6: Model parameters for 407015020

The high mass uncertainty is again caused by the unstable minimum noticeable in Figure 6.7 (b). The situation is similar to the contour for the observation number 407015010. The minimum at which the fit is settled is very unstable. The folded model in Figure 6.7 (a) appear to follow the data well, but the need to use the broken power law might have caused the uncertainty for the mass parameter of the BHSPEC model. Besides the high error of the mass estimate, the mass itself is quite high compared to the previous results even though the values overlap by the high error.

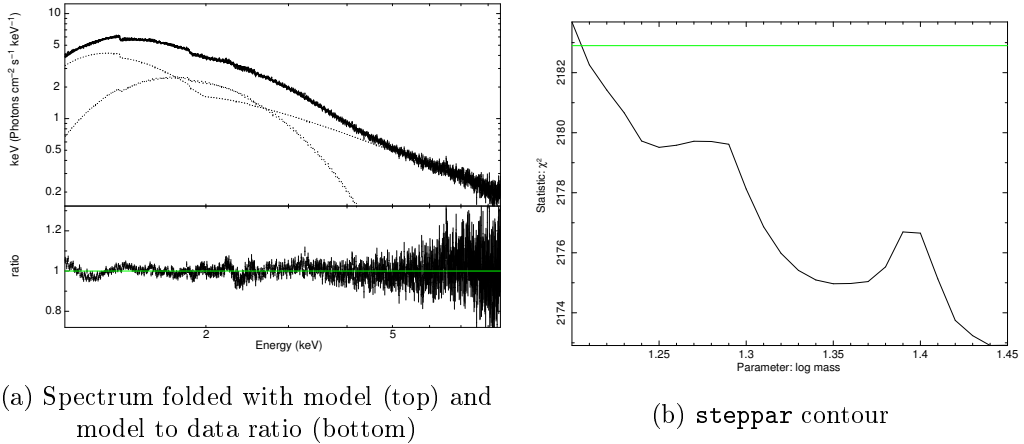


Figure 6.7: BHSPEC model applied to 407015020

The observation number 406013010 made by the Suzaku satellite provides a BH mass estimate that is on the contrary very low. The results of the fit are presented in Table 6.7 and despite the fact that the simple power law was sufficient for the fit, the χ^2 test still remained higher than desired. The resulting BH mass estimate is $4.7 \pm 2.1 M_{\odot}$. This result is very unlikely, as its lower boundary falls below the lower BH mass limit (or rather above the top mass limit of a neutron star). (Kalogera and Baym, 1996)

Model	Parameter	Input	Result	Error
TBabs	nH	–	0.295	0.15
BHSPEC	log mass	–	0.677	0.194
BHSPEC	log lumin	–	-1.952	0.194
BHSPEC	inc	0.640	0.640	–
BHSPEC	spin	–	0.876	0.15
BHSPEC	norm	–	41.991	18.335
POWERLAW	PhoIndex	–	2.223	0.029
POWERLAW	norm	–	5.876	0.346

$\chi^2_{\text{red}} = 2.855$ for 1096 DOF

Table 6.7: Model parameters for 406013010

Figure 6.8 (a) shows that only data for energy above 1.5 keV had to be used due to high disagreement with the model. This also prevented the exclusion of the instrument-related artefacts to avoid corrupting the shape of the spectrum. This might have been the cause for the high χ^2 test. Figure 6.8 (b) shows that the acquired `log mass` parameter is truly found in a local minimum of the contour. However, the low value of the BH mass estimate might be caused by the exclusion of the data below 1.5 keV as this part of the spectrum is created mostly by the thermal radiation.

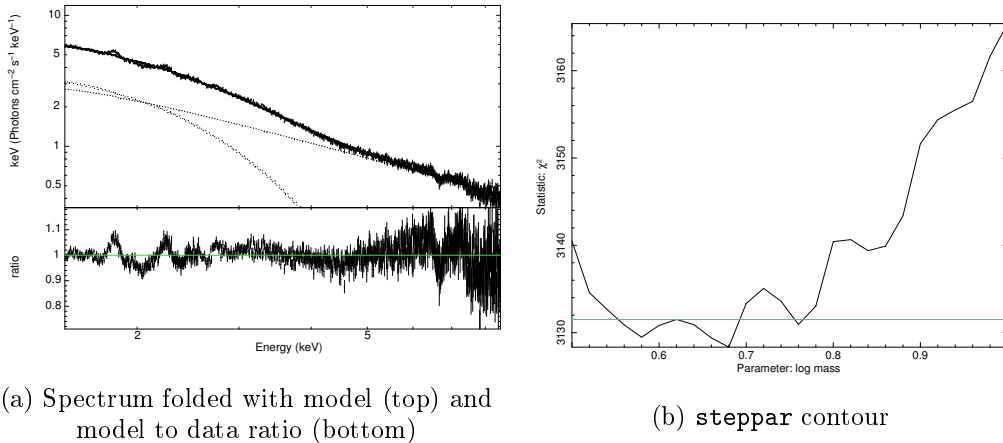


Figure 6.8: BHSPEC model applied to 406013010

The fitting of the spectrum from observation number 905006010 also required the exclusion of data below 1.5 keV. However, the `log mass` parameter is contrariwise quite high in comparison with the majority of the previous results. The BH mass estimate is $23.7 \pm 8.1 M_{\odot}$. The resulting parameters are shown in Table 6.8. The high χ^2 is caused by the presence of the emission line-like artefacts in the spectra. They were included in the fitting for the same reason as in the previous spectrum – to prevent disruption the shape of the spectrum.

Model	Parameter	Input	Result	Error
TBabs	nH	–	0.203	0.016
BHSPEC	log mass	–	1.375	0.147
BHSPEC	log lumin	–	-1.539	0.093
BHSPEC	inc	0.640	0.640	–
BHSPEC	spin	–	0.913	0.078
BHSPEC	norm	–	2.663	0.944
POWERLAW	PhoIndex	–	2.587	0.026
POWERLAW	norm	–	4.591	0.238

$\chi^2_{\text{red}} = 5.995$ for 1096 DOF

Table 6.8: Model parameters for 905006010

In both Figure 6.8 (a) and Figure 6.9 (a) there is a slight discontinuity noticeable at approximately 4.5 keV which might be caused by an occurrence of a weak reflection component. This is also supported by the fact that in every spectrum the iron line is present. Therefore, it is debatable whether the observations really capture the Cyg X-1 MQ in the thermal state or rather in the SPL state or in a intermediate state. The contour in Figure 6.9 (b) shows that the value of the `log mass` parameter was acquired at a not very stable point, as the χ^2 test value decreases for higher `log mass` values.

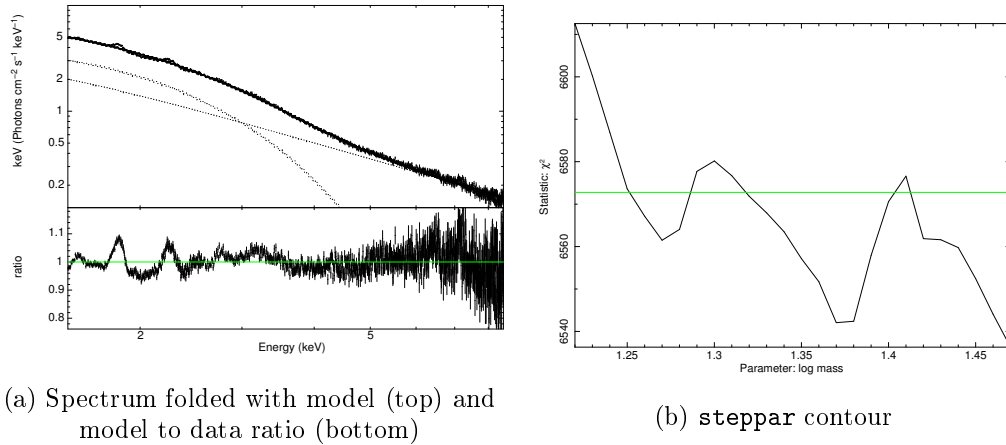


Figure 6.9: BHSPEC model applied to 905006010

The last two observations used with the BHSPEC model were carried out by the XMM Newton mission. The parameters obtained from the first one, 0202401101, are presented in Table 6.9. As well as for the last two Suzaku observations, the last XMM observation required exclusion of data below 1.5 keV. But the first one allowed including 1.0-1.5 keV bands even though the χ^2 remained rather high. The `log mass` parameter has a rather low error, but is quite high itself. The BH mass estimate is $21.6 \pm 4.5 M_{\odot}$. The spectrum together with the ratio is shown in Figure 6.10 (a).

Model	Parameter	Input	Result	Error
TBabs	nH	–	0.581	0.009
BHSPEC	log mass	–	1.335	0.091
BHSPEC	log lumin	–	-1.962	0.124
BHSPEC	inc	0.640	0.640	–
BHSPEC	spin	–	0.901	0.235
BHSPEC	norm	–	19.764	6.749
POWERLAW	PhoIndex	–	2.433	0.014
POWERLAW	norm	–	10.623	0.238

$\chi^2_{\text{red}} = 4.989$ for 126 DOF

Table 6.9: Model parameters for 0202401101

The model to data ratio in Figure 6.10 (a) shows that the model does not agree with the overall shape of the spectrum very well. Besides the iron line noticeable at 6.4 keV, there are long bands where the model does not follow the spectrum at all. The contour in Figure 6.10 (b) has a steep border from left side of the acquired `log mass` value, but is rather flat from the right side what might allow for even higher mass estimate to be acquired.

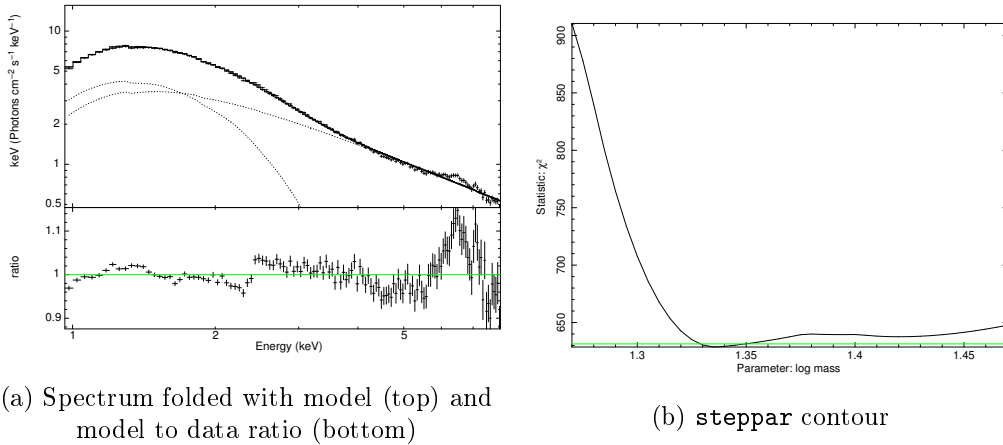


Figure 6.10: BHSPEC model applied to 0202401101

The last observation that the BHSPEC model was applied to was 0202401201.

The results are listed in Table 6.10. Features not contained in the model were not very prominent in this observation, so the χ^2 test is lower than for the previous XMM observation. However, data below 1.5 keV had to be excluded to stabilize the fit. As well as for the observation number 0202401101, the `log mass` parameter is rather high. The BH mass estimate is $21.1 \pm 9.8 M_{\odot}$.

Model	Parameter	Input	Result	Error
TBabs	nH	–	0.526	0.029
BHSPEC	log mass	–	1.325	0.201
BHSPEC	log lumin	–	-1.999	0.267
BHSPEC	inc	0.640	0.640	–
BHSPEC	spin	–	0.905	0.214
BHSPEC	norm	–	16.971	12.845
POWERLAW	PhoIndex	–	2.494	0.017
POWERLAW	norm	–	6.772	0.198

$\chi^2_{\text{red}} = 2.431$ for 125 DOF

Table 6.10: Model parameters for 0202401201

Figure 6.11 (a) shows the spectrum folded with the model and the model data ratio. In the ratio, a prominent iron line is observable. However, including this line into the model caused instability and drove the `log mass` value above 1.4 what is unreasonably high. Besides the iron line, the model seems to follow the spectrum below 6 keV quite well. The contour in Figure 6.11 (b) looks very similar to the one of 0202401101. Adding iron line to the model caused the right side of the contour to drop and dragged the minimum to the right of the current one.

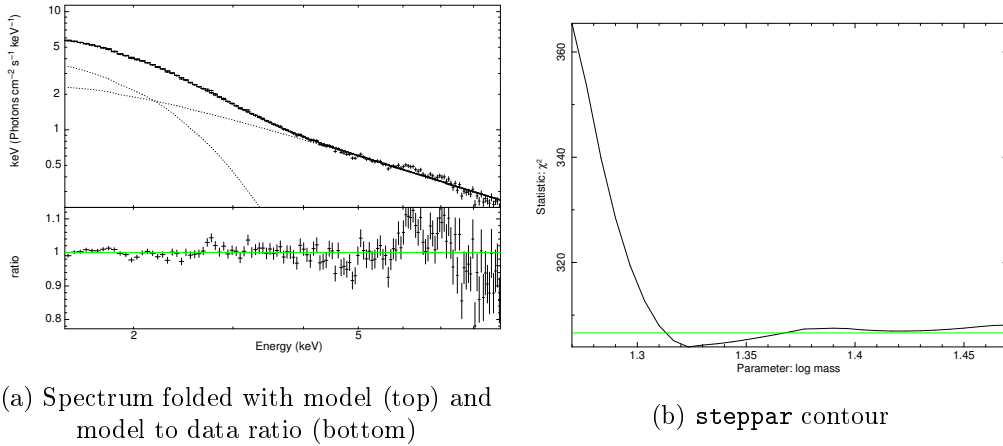


Figure 6.11: BHSPEC model applied to 0202401201

Results

The aim of this work was to present a brief introduction about MQs, to provide future readers with guides on retrieving and processing X-ray data and to make new estimates of parameters of selected MQs. The objects that were selected for this work were GX 339-4 and Cygnus X-1. The idea was to create a procedure that would be applied to the GX 339-4 MQ and then test it on the Cygnus X-1 MQ.

The results obtained for the GX 339-4 MQ are presented in Table 7.1. There is an estimate of the BH mass and distance to the MQ for each observation. The inclination of the system was extracted from the RELXILL model applied to the observation number 401068010. The estimated inclination is **50.2±2 degrees**. This inclination was used together with the mass function of GX 339-4 to determine the mass of the BH. The inclination was also used as an input for the BHSPEC model, from which the `log mass` parameter was extracted as another BH mass estimate.

Observation	Mission	M_{BH} (M_{\odot})	ΔM_{BH} (M_{\odot})	d (kpc)	Δd (kpc)
401068010 ^a	Suzaku	15.0	2.5	6.0	0.3
401068010	Suzaku	11.2	4.4	13.0	3.2
0093562701	XMM	19.6	9.7	5.4	1.6
0410581201	XMM	14.1	5.4	5.9	2.2
0410581301	XMM	14.7	8.0	6.8	2.7
0410581701	XMM	15.7	8.2	19.6	8.0

Table 7.1: Results obtained for the GX 339-4 MQ. The “a” denotes the results derived from the RELXILL model, rest is from the BHSPEC model.

The distance to the object was calculated from the normalisation parameters of the models. The RELXILL model does not provide information about the distance, so the distance was computed from the *norm* parameter of the DISKBB model from Table 5.3. It is defined as $norm = ((R_{\text{in}}/\text{km})/(d/10 \text{ kpc}))^2 \cos i$. The R_{in} parameter was to ISCO and the mass derived from the mass function was used. The rest of the distance estimates in Table 7.1 was derived from the BHSPEC model’s normalisation parameter defined $norm = (10 \text{ kpc}/d)^2$.

The next step was to repeat the procedure with another object to verify the results obtained with the GX 339-4 MQ. The parameters acquired for the Cygnus X-1 are presented in Table 7.2 for each used observation. The inclination was derived from the observation number 407072010 using the RELXILL model. The inclination estimate is **52.2±2 degrees**. This value was again used together with the mass function in order to obtain the BH mass estimate, which is presented in Table 7.2 as the first entry. The inclination was used as an input for the BHSPEC model, from which the other BH mass estimates in the table were derived.

Observation	Mission	M_{BH} (M_{\odot})	ΔM_{BH} (M_{\odot})	d (kpc)	Δd (kpc)
407072010 ^a	Suzaku	7.3	2.6	0.1	0.02
407072010	Suzaku	7.5	4.3	1.8	0.7
407015010	Suzaku	7.8	–	5.4	–
407015020	Suzaku	23.5	17.1	5.9	2.6
406013010	Suzaku	4.8	2.2	1.5	0.3
905006010	Suzaku	23.7	8.1	6.1	1.1
0202401101	XMM	21.6	4.5	2.3	0.4
0202401201	XMM	21.1	9.8	2.4	0.9

Table 7.2: Results obtained for the Cygnus X-1 MQ. The “a” denotes the results derived from the RELXILL model, rest is from the BHSPEC model.

The distance to the MQ was computed in the same way as for the GX 339-4 MQ. The inclination for the first entry in Table 7.2 was derived from the DISKBB model and the rest was derived from the BHSPEC model. The observation number 407015010 lacks the error values for both BH mass and distance estimates. These values were omitted because of their size, which exceeded the estimates.

Discussion

The biggest problem when applying models to data is that the models usually correspond only to certain spectral components that need to be contained in the spectra and respond to the state of an object. If an object does not exhibit a reflection component, applying the RELXILL model will not provide reasonable information. The identification of the state of an object is crucial in deriving estimates of its parameters.

The results presented in Table 7.1 may appear somewhat incorrect compared to the most recent estimates listed in Chapter 2. Despite some diversity, the BH mass estimates in Table 7.1 mostly overlap thanks to their errors, but are a bit larger than the recently published values. However, the estimates derived from the BHSPEC model are in agreement with the BH mass estimate derived from the mass function using the system inclination. The inclination falls within the 20–60 degrees limit and is quite close to the recently published inclination of 48 ± 1 degrees (García et al., 2015). Therefore the inclination and the BH mass estimate of $15 \pm 4 M_{\odot}$ can be considered suitable.

As for the distance to the GX 339-4 MQ, Table 7.1 contains a distance derived from the *norm* parameter of the DISKBB model and distances derived from the *norm* parameter of the BHSPEC model. Except two cases, the values span around $\sim 6\text{--}7$ kpc with the error of ~ 2 kpc. This is in good agreement with recently published values, e.g. 8.4 kpc (Parker et al., 2015) or ≥ 7 kpc (Zdziarski et al., 2004).

The spin of the BH of the GX 339-4 is generally considered to be nearly maximal, which corresponds to the results acquired from both the RELXILL model and the BHSPEC model. Except for the value presented in Table 5.4. The spin estimation requires the MQ to be in the thermal or the SPL state as the spin is determined from the R_{in} of the disc. In the cases when the disc is not extended down to the ISCO, the spin estimate cannot be acquired correctly. The spin of the BH contained within GX 339-4 was estimated to be ≥ 0.98 .

The Cygnus X-1 MQ was supposed to be used as a verification for the procedure used. However, the results derived for the Cygnus X-1 MQ appear to differ from the recently published values. This does not necessarily mean that the procedure is incorrect. It is important to assess everything that might have affected the process.

The most important aspect that needs to be considered is the fact that the Cygnus X-1 MQ is a HMXB. The GX 339-4 is on the contrary a LMXB. That means that the procedure applied to the latter does not necessarily need to work with the former the same way. When studying a HMXB, the absorption arises not only from the interstellar matter, but can contain a distinctive portion related to the MQ itself. The hydrogen column density of the Cygnus X-1 MQ is highly variable and can be related to the orbital movement of the components of the system. (Grinberg et al., 2015) The stream of the material from the donor star can be much more widespread than in the case of a LMXB and create regions of concentrated mass crossing the LOS. As the variability affects mostly the energies related to the disc component of the spectrum, an uncertain determination of the absorption may corrupt the fitting of the thermal component.

The inclination found in the recent articles is ~ 30 degrees. (Ziółkowski, 2014) However, the inclination derived from the RELXILL model is **52.2 ± 2 degrees**, which is much more than generally accepted values. The combination of the 30 degrees inclination and the mass function of the Cygnus X-1 MQ provides an unreasonably high mass of $29 M_{\odot}$. The BH mass estimate derived from the 52.2 degrees inclination is **$7.3 \pm 2.6 M_{\odot}$** . Unfortunately the other BH mass estimates presented in Table 7.2 vary a lot. The estimates range from $4 M_{\odot}$ up to $24 M_{\odot}$. The uncertainty of determining the mass of the BH can be assigned to improper determination of the nH parameter of the absorption component.

The spin of the BH within the Cygnus X-1 MQ is thought to be high, but a wide range of spins was acquired when applying the BHSPEC model. This problem may again arise from the variable absorption component. Moreover, the observations used with the model do not necessarily need to be captured when the MQ was in the thermal state but rather in a similar intermediate state.

The distance of this object is well-established with parallax measurement and therefore is very reliable. It was measured to be $1.86^{+0.12}_{-0.11}$ kpc (Reid et al., 2011). However, only a few estimates of the distance in Table 7.2 are close to this value. Most values are very different.

The parameters acquired for the Cygnus X-1 MQ vary a lot from the recently published values. However, this fact does not make the procedure applied to the GX 339-4 MQ incorrect. It only proves that all the MQs cannot be addressed in the same way as they differ in many aspects. To verify the procedure, more MQs should be tested. Moreover, repeating the same steps for the same type of a MQ would be appropriate.

Future work on this approach should include more objects to be studied. Mainly objects that resemble each other or fall into the same category. As for the GX 339-4 MQ, objects like GS 1354-64 or XTE J1655-40 could be more suitable than the Cygnus X-1 MQ. Furthermore, in addition to spectral analysis, timing analysis could provide more insight into the state of a MQ and improve the application of an appropriate model to determine the system parameters.

References

- K. A. Arnaud. XSPEC: The First Ten Years. In G. H. Jacoby and J. Barnes, editors, *Astronomical Data Analysis Software and Systems V*, volume 101 of *Astronomical Society of the Pacific Conference Series*, page 17, 1996.
- G. Bao, P. Hadrava, and E. Ostgaard. Multiple images and light curves of an emitting source on a relativistic eccentric orbit around a black hole. *The Astrophysical Journal*, 425:63–71, April 1994. doi: 10.1086/173963.
- T. Chen. The determination of the GX 339-4’s mass based on its 2010 outburst. In G. E. Romero, R. A. Sunyaev, and T. Belloni, editors, *Jets at All Scales*, volume 275 of *IAU Symposium*, pages 327–328, February 2011. doi: 10.1017/S1743921310016339.
- S. W. Davis, O. M. Blaes, I. Hubeny, and N. J. Turner. Relativistic Accretion Disk Models of High-State Black Hole X-Ray Binary Spectra. *The Astrophysical Journal*, 621:372–387, March 2005. doi: 10.1086/427278.
- R. Fender. Relativistic Outflows from X-ray Binaries (‘Microquasars’). In A. W. Guthmann, M. Georganopoulos, A. Marcowith, and K. Manolakou, editors, *Relativistic Flows in Astrophysics*, volume 589 of *Lecture Notes in Physics*, Berlin Springer Verlag, page 101, 2002.
- J. Frank, A. King, and D. J. Raine. *Accretion Power in Astrophysics: Third Edition*. UK: Cambridge University Press, January 2002.
- J. García, T. Dauser, C. S. Reynolds, T. R. Kallman, J. E. McClintock, J. Wilms, and W. Eikmann. X-Ray Reflected Spectra from Accretion Disk Models. III. A Complete Grid of Ionized Reflection Calculations. *The Astrophysical Journal*, 768:146, May 2013. doi: 10.1088/0004-637X/768/2/146.
- J. A. García, J. F. Steiner, J. E. McClintock, R. A. Remillard, V. Grinberg, and T. Dauser. X-Ray Reflection Spectroscopy of the Black Hole GX 339–4: Exploring the Hard State with Unprecedented Sensitivity. *The Astrophysical Journal*, 813: 84, November 2015. doi: 10.1088/0004-637X/813/2/84.
- D. R. Gies, C. T. Bolton, R. Fender, A. Herrero, T. C. Hillwig, L. Kaper, M. V. McSwain, J. Thomson, D. J. Wallace, and P. J. Wiita. Wind Accretion and State

- Transitions in the Black Hole Binary Cyg X-1. In *American Astronomical Society Meeting Abstracts*, volume 35 of *Bulletin of the American Astronomical Society*, page 1332, December 2003.
- V. Grinberg, M. A. Leutenegger, N. Hell, K. Pottschmidt, M. Böck, J. A. García, M. Hanke, M. A. Nowak, J. O. Sundqvist, R. H. D. Townsend, and J. Wilms. Long term variability of Cygnus X-1. VII. Orbital variability of the focussed wind in Cyg X-1/HDE 226868 system. *Astronomy & Astrophysics*, 576:A117, April 2015. doi: 10.1051/0004-6361/201425418.
- R. I. Hynes, D. Steeghs, J. Casares, P. A. Charles, and K. O'Brien. Dynamical Evidence for a Black Hole in GX 339-4. *The Astrophysical Journal*, 583:L95–L98, February 2003. doi: 10.1086/368108.
- V. Kalogera and G. Baym. The Maximum Mass of a Neutron Star. *Astrophysical Journal Letters*, 470:L61, October 1996. doi: 10.1086/310296.
- R. M. Ludlam, J. M. Miller, and E. M. Cackett. Reapproaching the Spin Estimate of GX 339-4. *The Astrophysical Journal*, 806:262, June 2015. doi: 10.1088/0004-637X/806/2/262.
- T. H. Markert, C. R. Canizares, G. W. Clark, W. H. G. Lewin, H. W. Schnopper, and G. F. Sprott. Observations of the Highly Variable X-Ray Source GX 339-4. *The Astrophysical Journal*, 184:L67, September 1973. doi: 10.1086/181290.
- J. M. Miller. Relativistic X-Ray Lines from the Inner Accretion Disks Around Black Holes. *Annual Review of Astronomy & Astrophysics*, 45:441–479, September 2007. doi: 10.1146/annurev.astro.45.051806.110555.
- K. Mitsuda, H. Inoue, K. Koyama, K. Makishima, M. Matsuoka, Y. Ogawara, K. Suzuki, Y. Tanaka, N. Shibasaki, and T. Hirano. Energy spectra of low-mass binary X-ray sources observed from TENMA. *Publications of the Astronomical Society of Japan*, 36:741–759, 1984.
- S. Motta, T. Muñoz-Darias, P. Casella, T. Belloni, and J. Homan. Low-frequency oscillations in black holes: a spectral-timing approach to the case of GX 339-4. *MNRAS*, 418:2292–2307, December 2011. doi: 10.1111/j.1365-2966.2011.19566.x.
- J. A. Orosz, J. E. McClintock, J. P. Aufdenberg, R. A. Remillard, M. J. Reid, R. Narayan, and L. Gou. The Mass of the Black Hole in Cygnus X-1. *Astrophysical Journal*, 742:84, December 2011. doi: 10.1088/0004-637X/742/2/84.
- A. Paizis, K. Ebisawa, H. Takahashi, T. Dotani, T. Kohmura, M. Kokubun, J. Rodriguez, Y. Ueda, R. Walter, S. Yamada, K. Yamaoka, and T. Yuasa. Broad-Band Spectrum of the Black Hole Candidate IGR J17497-2821 Studied with Suzaku. *Publications of the Astronomical Society of Japan*, 61:S107–S113, January 2009. doi: 10.1093/pasj/61.sp1.S107.

- M. L. Parker, A. C. Fabian, G. Matt, K. I. I. Koljonen, E. Kara, W. Alston, D. J. Walton, A. Marinucci, L. Brenneman, and G. Risaliti. Revealing the X-ray variability of AGN with principal component analysis. *MNRAS*, 447:72–96, February 2015. doi: 10.1093/mnras/stu2424.
- M. L. Parker, J. A. Tomsick, J. A. Kennea, J. M. Miller, F. A. Harrison, D. Barret, S. E. Boggs, F. E. Christensen, W. W. Craig, A. C. Fabian, F. Fuerst, V. Grinberg, C. J. Hailey, P. Romano, D. Stern, D. J. Walton, and W. W. Zhang. NuSTAR and Swift observations of the very high state in GX 339-4: Weighing the black hole with X-rays. *ArXiv e-prints*, March 2016.
- M. J. Reid, J. E. McClintock, R. Narayan, L. Gou, R. A. Remillard, and J. A. Orosz. The Trigonometric Parallax of Cygnus X-1. *The Astrophysical Journal*, 742:83, December 2011. doi: 10.1088/0004-637X/742/2/83.
- R. A. Remillard and J. E. McClintock. X-Ray Properties of Black-Hole Binaries. *Annual Review of Astronomy & Astrophysics*, 44:49–92, September 2006. doi: 10.1146/annurev.astro.44.051905.092532.
- H. Sreehari, N. Iyer, and A. Nandi. Constraining the mass of Galactic black hole GX 339-4. In *Astronomical Society of India Conference Series*, volume 12 of *Astronomical Society of India Conference Series*, 2015.
- J. Svoboda, M. Dovciak, R. W. Goosmann, and V. Karas. Comparison of Relativistic Iron Line Models. *ArXiv e-prints*, January 2009.
- J. A. Tomsick, M. A. Nowak, M. Parker, J. M. Miller, A. C. Fabian, F. A. Harrison, M. Bachetti, D. Barret, S. E. Boggs, F. E. Christensen, W. W. Craig, K. Forster, F. Fürst, B. W. Grefenstette, C. J. Hailey, A. L. King, K. K. Madsen, L. Natalucci, K. Pottschmidt, R. R. Ross, D. Stern, D. J. Walton, J. Wilms, and W. W. Zhang. The Reflection Component from Cygnus X-1 in the Soft State Measured by NuSTAR and Suzaku. *Astrophysical Journal*, 780:78, January 2014. doi: 10.1088/0004-637X/780/1/78.
- A. A. Zdziarski, M. Gierliński, J. Mikołajewska, G. Wardziński, D. M. Smith, B. A. Harmon, and S. Kitamoto. GX 339-4: the distance, state transitions, hysteresis and spectral correlations. *MNRAS*, 351:791–807, July 2004. doi: 10.1111/j.1365-2966.2004.07830.x.
- S.-N. Zhang. Black hole binaries and microquasars. *Frontiers of Physics*, 8:630–660, December 2013. doi: 10.1007/s11467-013-0306-z.
- J. Ziółkowski. Determination of the masses of the components of the HDE 226868/Cyg X-1 binary system. *MNRAS*, 440:L61–L65, May 2014. doi: 10.1093/mnrasl/slu002.

Electronic references and sources

[e1] <http://www.universetoday.com>

[e2] <http://mintaka.sdsu.edu/faculty/orosz/web/>

[e3] <https://heasarc.gsfc.nasa.gov/lheasoft/download.html>

[e4] https://heasarc.gsfc.nasa.gov/docs/suzaku/aehp_about.html

[e5] <http://heasarc.gsfc.nasa.gov/cgi-bin/W3Browse/w3browse.pl>

[e6] ftp://legacy.gsfc.nasa.gov/suzaku/doc/general/suzaku_abc_guide.pdf

[e7] <http://www.cosmos.esa.int/web/xmm-newton/technical-details>

[e8] <http://nxsa.esac.esa.int/nxsa-web/#search>

[e9] <http://www.cosmos.esa.int/web/xmm-newton/download-and-install-sas>

Appendix A - Spectrum extraction

MOS in imaging mode

```
evselect table=mos1U002-clean.fits withspectrumset=yes \  
  spectrumset=MOSsource_spectrum.fits energycolumn=PI \  
  spectralbinsize=5 withspecranges=yes specchannelmin=0 \  
  specchannelmax=11999 expression='#XMMEA_EM && \  
  (PATTERN<=12) && ((X,Y) IN circle(25393.5,23814.5,500))'  
evselect table=mos1U002-clean.fits withspectrumset=yes \  
  spectrumset=MOSbackground_spectrum.fits energycolumn=PI \  
  spectralbinsize=5 withspecranges=yes specchannelmin=0 \  
  specchannelmax=11999 expression='#XMMEA_EM && \  
  (PATTERN<=12) && ((X,Y) IN annulus(30360.5,28400.5,650,1000))'  
rmfgen spectrumset=MOSsource_spectrum.fits rmfset=MOS.rmf  
arfgen spectrumset=MOSsource_spectrum.fits arfset=MOS.arf \  
  withrmfset=yes rmfset=MOS.rmf badpixlocation=MOSclean.fits \  
  detmctype=psf  
specgroup spectrumset=MOSsource_spectrum.fits mincounts=25 \  
  oversample=3 rmfset=MOS.rmf arfset=MOS.arf \  
  backgndset=MOSbackground_spectrum.fits \  
  groupedset=MOS_spectrum_grp.fits
```

PN in imaging mode

```
evselect table=EPICclean.fits withspectrumset=yes \  
  spectrumset=PNsource_spectrum.fits energycolumn=PI \  
  spectralbinsize=5 withspecranges=yes specchannelmin=0 \  
  specchannelmax=11999 expression='(FLAG==0) && \  
  (PATTERN<=4) && ((X,Y) IN circle(25393.5,23814.5,500))'  
evselect table=EPICclean.fits withspectrumset=yes \  
  spectrumset=PNbackground_spectrum.fits energycolumn=PI \  
  spectralbinsize=5 withspecranges=yes specchannelmin=0 \  
  specchannelmax=11999 expression='(FLAG==0) && \  
  (PATTERN<=4) && ((X,Y) IN annulus(30360.5,28400.5,650,1000))'
```

```

rmfgen spectrumset=PNsource_spectrum.fits rmfset=PN.rmf
arfgen spectrumset=PNsource_spectrum.fits arfset=PN.arf \
  withrmfset=yes rmfset=PN.rmf \
  badpixlocation=PNclean.fits detmctype=psf
specgroup spectrumset=PNsource_spectrum.fits \
  mincounts=25 oversample=3 rmfset=PN.rmf arfset=PN.arf \
  backgndset=PNbackground_spectrum.fits \
  groupedset=PN_spectrum_grp.fits

```

PN in timing mode

```

evselect table=EPICclean.fits withspectrumset=yes \
  spectrumset=PNsource_spectrum.fits energycolumn=PI \
  spectralbinsize=5 withspecranges=yes specchannelmin=0 \
  specchannelmax=20479 expression='(FLAG==0) && \
  (PATTERN<=4) && (RAWX>=29) && (RAWX<=47)'
evselect table=EPICclean.fits withspectrumset=yes \
  spectrumset=PNbackground_spectrum.fits energycolumn=PI \
  spectralbinsize=5 withspecranges=yes specchannelmin=0 \
  specchannelmax=20479 expression='(FLAG==0) && \
  (PATTERN<=4) && (RAWX>=3) && (RAWX<=5)'
backscale spectrumset=PNsource_spectrum.fits \
  badpixlocation=EPICclean.fits
backscale spectrumset=PNbackground_spectrum.fits \
  badpixlocation=EPICclean.fits
rmfgen spectrumset=PNsource_spectrum.fits rmfset=PN.rmf
arfgen spectrumset=PNsource_spectrum.fits arfset=PN.arf \
  withrmfset=yes rmfset=PN.rmf \
  badpixlocation=EPICclean.fits detmctype=psf
specgroup spectrumset=PNsource_spectrum.fits \
  mincounts=25 oversample=3 rmfset=PN.rmf arfset=PN.arf \
  backgndset=PNbackground_spectrum.fits \
  groupedset=PN_spectrum_grp.fits

```

PN in burst mode

The only difference in the procedure for the burst mode is an additional `RAWY` condition for the `evselect` command for both source and background spectrum.

```

expression='(FLAG==0) && (PATTERN<=4) && \
  (RAWX>=3) && (RAWX<=5) && (RAWY<=140)'

```